GEOLOGICA CARPATHICA, OCTOBER 2023, 74, 5, 387–406 https://doi.org/10.31577/GeolCarp.2023.23

The composite zircon–xenotime–monazite–allanite assemblage in the leucogranite from the Low Tatra Pluton, Western Carpathians: Interplay of melts and fluids

MARIA MARASZEWSKA[1, ✉], IGOR BROSKA[2], SERGIY KURYLO[1] and PATRIK KONEČNÝ[3]

[1]Earth Science Institute, Slovak Academy of Sciences, Ďumbierska cesta 1, 974 01 Banská Bystrica, Slovakia; ✉maraszewska@savbb.sk
[2]Earth Science Institute, Slovak Academy of Sciences, Dúbravská cesta 9, 840 05 Bratislava, Slovakia
[3]State Geological Institute of Dionýz Štúr, Mlynská dolina 1, 817 04 Bratislava, Slovakia

(Manuscript received July 27, 2023; accepted in revised form November 25, 2023; Associate Editor: Peter Bačík)

Abstract: The highly peraluminous Zámostská Hoľa leucogranite (ZHG) forms a small, dyke-like body within the granodiorites of the Prašivá type in the composite, 353–351 myr Low Tatra Pluton (LTP), Central Western Carpathians, Slovakia. The ZHG fabric recorded syn-magmatic brecciation, multiple influxes of fluid-rich melt, and fluid-rock interaction. The accessory mineral assemblage includes zircon, xenotime-(Y), monazite-(Ce) and allanite-(Ce). The zircon in the ZHG shows very low Zr/Hf and Th/U; apparently, primary zircon is euhedral, oscillatory zoned and P, Al, Ca, Fe, U, Y, HREE-rich; however, most of the zircon grains are to variable extents altered by dissolution–reprecipitation process, and show depletion or redistribution of trace elements within the crystal. The xenotime-(Y) is spatially associated with zircon and varies from the euhedral, igneous-like to strongly irregular secondary grains formed from the zircon dissolution in the presence of P-bearing fluid. Some zircon and xenotime-(Y) grains are high in As. The monazite-(Ce) shows morphology typical for early-magmatic origin, and alteration is restricted to huttonite-enriched, U, Ca, Y-depleted rims and patches; however, the entire crystals are unusually high in F up to 0.8 wt%. The monazite-(Ce), followed by the trace element-rich zircon and euhedral xenotime-(Y), crystallized from peraluminous, F, U, Y+HREE-enriched melt and resemble ones from highly fractionated granites or pegmatites. The alteration of primary accessory minerals and formation of the secondary xenotime-(Y) is related to an influx of alkali-enriched, fluid-dominated magma. The reaction of REE in fluid with brecciated and altered plagioclase and micas led to the local formation of secondary allanite-(Ce). The magmatic age of the ZHG monazite is 345±2.5 Ma and emphasizes its formation in the final stage of the prolonged evolution of the LTP; but whether the leucogranite represents residual differentiates of the magma of hosting Prašivá type, or independent magmatic pulses, remains an unresolved issue. The exceptional accessory phases assemblage records mineral–melt–fluid interactions in the late magmatic-hydrothermal transition, which is the critical ore-forming phase, and overall characteristics of the ZHG minerals shares attributes of those in the fertile intrusions and provides arguments for the close relationship between the composite magmatism and the ore petrogenesis in the LTP.

Keywords: Western Carpathians, granite, magmatic–hydrothermal transition, accessory minerals in ore exploration, zircon, xenotime

Introduction

The highly fractionated granitic melts can be formed by low-degree anatexis of (mostly) upper crustal sources, but also in the final stages of evolution of siliceous magmas, by their extensive differentiation and proceeding with a decrease of temperature and pressure during ascent and emplacement. The residual melts are geochemically evolved, which is expressed by high SiO_2, Al_2O_3 and alkali content, ASI>1.0 (Alumina Saturation Index), enrichment in the incompatible elements such as REE, Y, U, Hf, Zr, Nb, Ta (Simons et al. 2017) and fluids, as water and halogens, which can reach several wt% in ore-bearing suites (Halter & Webster 2004; Dolejš & Zajacz 2018). When melt approaches its solidus, the volatiles are exsolved, marking the magmatic–hydrothermal transition, which is the key process for the development of pegmatite systems and various associations of ore mineralization and metasomatic reactions (Halter & Webster 2004). Accessory minerals in granitoids – such as zircon, apatite, or monazite – are excellent tools in petrochronological and petrogenetic studies (Watson & Harrison 1984; Wark & Miller 1993; Hoskin et al. 2000; Broska et al. 2012). The specific composition of highly fractionated melts and related volatiles has impact on the assemblages and chemistry of the magmatic and hydrothermal accessory phases and induces their alteration, differentiating them from those in "common" granitoids (Förster 1998a, b; Erdmann et al. 2012; Breiter et al. 2014; Broska & Kubiš 2018), which contributes to their application as tracers of the ore-forming processes (Schaltegger et al. 2005; Fu et al. 2009; van Lichtervelde et al. 2009; Förster et al. 2011).

This paper refers to the specific accessory mineral assemblage in a small leucogranite body from the Low Tatra Mts. (Western Carpathians); the investigated mineral assemblage

includes zircon, xenotime-(Y), monazite-(Ce) and allanite-(Ce). Each of the mineral phases shows microtextural and compositional peculiarities, suggesting multistage formation in the late magmatic to hydrothermal stages. This study contributes to the understanding of the complex response of the accessory phases during the final stages of evolution in the felsic suites, with possible metallogenic implications for the Low Tatra Mts. pluton.

Geological outline

The crystalline basement of the Central Western Carpathians (CWC) represents a segment of an orogenic crust of the European Variscan belt, which was dismembered and rearranged during the Alpine orogeny, and together with Mesozoic and Cenozoic sedimentary successions was involved into crustal-scale nappe system within the Tatric, Veporic and Gemeric superunits (Plašienka et al. 1997; Hók et al. 2019). The crystalline basement of the CWC of the Tatric Superunit (TS) is exposed in horst-like massifs, with the cores formed by Variscan granitoid plutons, mantled by a metaigneous-metasedimentary complex, encompassing high-grade Lower Unit and low/medium-grade Upper Unit (Bezák et al. 1997).

Most of the granitoids in the TS show chemical and isotopic systematic suggesting derivation from multiple sources (Kohút & Nabelek 2008; Magna et al. 2010); however, on the basis of their typology, they can be subdivided into two groups (Petrík & Broska 1994; Petrík & Kohút 1997; Broska & Uher 2001). The first group ("I-type affiliated") are biotite (±amphibole) tonalites–granodiorites, which are metaluminous to moderately peraluminous, and allanite and magnetite-bearing, and resemble ACG to KCG suites (Amphibole-bearing Calc-alkaline – High-K Calc-alkaline Granitoids acc. to geochemical criteria of Bonin et al. 2020 and references therein), and originate from water-rich magmas from intermediate–mafic metaigneous±mantle sources. The second group ("S-type affiliated") shows attributes of (post)-collisional granites of the CPG–MPG types (Cordierite-bearing Peraluminous–Muscovite-bearing Peraluminous Granitoids; Bonin et al. 2020) derived mostly from metasedimentary, and/or felsic metaigneous sources, and includes peraluminous, leucocratic, biotite or two-mica granodiorites-granites, containing accessory monazite and ilmenite. The melting of a heterogeneous crust by mantle upwelling, rapid exhumation, and transpression was induced by slab break-off (Broska et al. 2022), and lasted from very late Devonian to middle Carboniferous in subduction-(post)collision regime (Broska et al. 2013; Kohút & Larionov 2021; Catlos et al. 2022). However, the paleogeographic position of the CWC granites with respect to other segments of the European Variscides is still not well constrained.

The Low Tatra Mts. are an asymmetric, E–W elongated horst consisting of a composite granitoid pluton in the N part (the Low Tatra Pluton itself; LTP) and an orthogneiss-dominated metamorphic complex in the S part (Fig. 1B, C). The LTP shows zonation, manifested by coexistence of several compositionally different granitoid types (Biely et al. 1992; Maraszewska et al. 2022; Fig.1). The two dominant granitic types include "Ďumbier" tonalite–granodiorite in the SE-E zone, and strongly heterogeneous "Prašivá" granodiorite–granite in the NW-W zone (subdivided into weakly porphyritic "Aln-Prašivá Subtype" and porphyritic "Mnz-Prašivá subtype"; Maraszewska et al. 2019a, 2022). The volume fraction of mafic-intermediate rocks (small diorite bodies and mafic microgranular enclaves in both granite types) is insignificant within the whole LTP. The dominant granitoid types in the LTP show hybrid character, as they are weakly to moderately peraluminous, high-K calc-alkaline to alkali-calcic, high Ba, Sr, LREE, Sr/Y and La/Yb, and the sequence Ďumbier–Aln-Prašivá–Mnz-Prašivá subtype reflects evolution from KCG to CPG-like character (Maraszewska et al. 2022). The geochronological systematics of zircon and monazite in the major granitoid types in the LTP show a composite record, extending from early Tournaisian to early Visean, with culmination between 353±2–352±2–351±3 Ma (average zircon ages of Ďumbier–Aln-Prašivá–Mnz-Prašivá suites, respectively; Maraszewska et al. 2022) implying a successive, prolonged growth of the pluton in post-collisional setting, and evolving from the lower- to middle/upper crustal sources magmas through time (Maraszewska et al. 2021, 2022).

Muscovite or two-mica (leuco)granites s.s. occur in several localities within the LTP. They are formed in various sizes (from several metres to kilometres; Fig. 1C), tectonically-controlled intrusions, enclosed by Ďumbier and Prašivá granite types, as well as within metamorphic rocks and migmatites. In the NE area of the metamorphic complex, muscovite-bearing bodies of "Králička type granite" are hosted by migmatized orthogneisses (Kohút &Nabelek 2008) and biotite–garnet leucogranites were documented in Šifrová dolina (Petrík & Konečný 2009); small, isolated leucogranite body is also surrounded by exotic low-grade phyllites in Klinisko–Malé Železné W–Mo deposit. Although the leucogranites in the LTP are poorly documented, and individual bodies show differences in fabric, mineralogy and chemistry, they share the signature of MPG to CPG, as they are high-silica (>70 wt% SiO_2), high peraluminous, and lower in FeO_t, MgO, TiO_2, Sr, Ba, Zr and REE's than the major granitoid types in the LTP. The granite hosted by metamorphic rocks represents a product of the anatexis of the orthogneisses and/or metasediments in Visean (monazite ages of the garnet leucogranite; Petrík & Konečný 2009). However, the Králička type (and isotopically and chemically similar "Chopok two-mica granite"; Burda et al. 2020) are likely products of pre-Variscan crustal melting. The origin of leucogranite bodies inboard the pluton is unresolved; the geochronological record in zircon is ambiquitous, and the datings are scattered from Fammenian/Tournaisian to late Visean, whereas monazite provided ages ca. 350 Ma (Maraszewska et al. 2021). The pegmatites and aplites are widespread within the LTP; barren two feldspar pegmatites are most common (Dávidová 1978), but some of the bodies within the Prašivá granodiorite contain composite Nb–Ta–Ti mineralization (Uher et al. 1998a, b) and beryl (Pitoňák & Janák

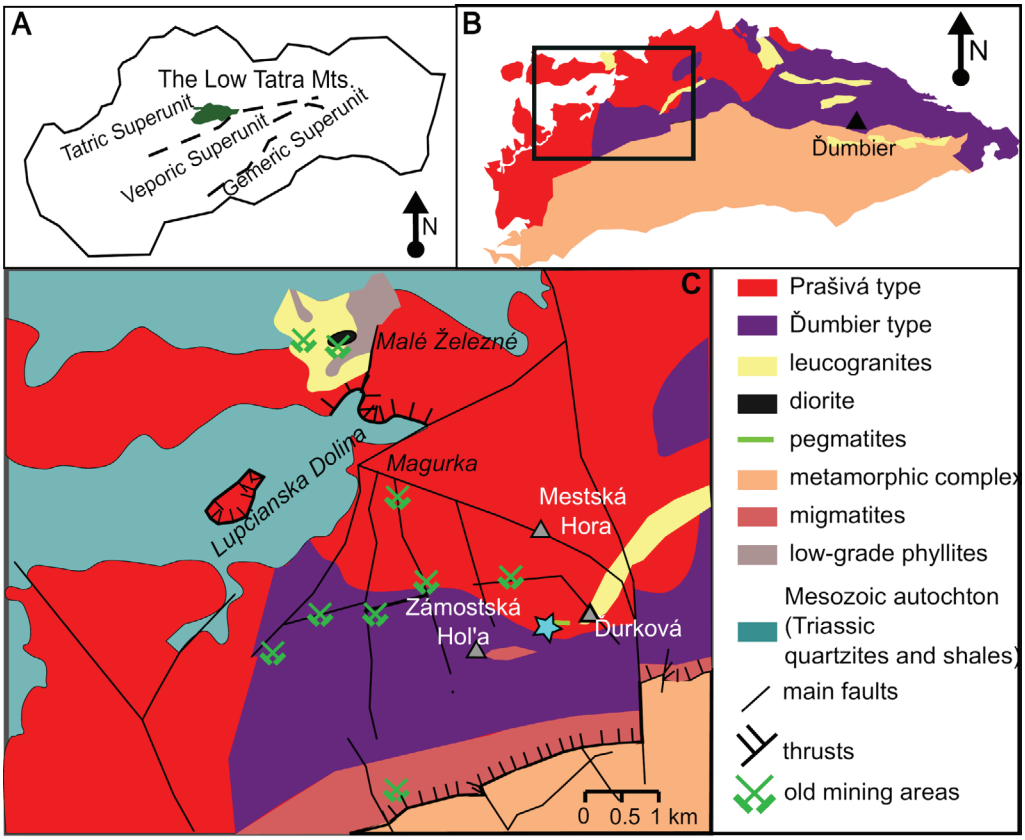

Fig. 1. A — Location of the Low Tatra Mts. **B** — Simplified map of the crystalline basement in the Low Tatra (after Biely et al. 1992; Maraszewska et al. 2022). **C** — Geological map of the investigated part of the Low Tatra Mts with marked mining excavations (after Biely et al. 1992; Chovan et al. 1995; Maraszewska et al. 2022) – blue star point to the occurrence of the Zámostská Hoľa leucogranite (ZHG) body.

1983) and were identified as beryl-columbite subtype of the LCT pegmatites (Uher et al. 1998a).

The studied Zámostská Hoľa leucogranite (ZHG) crops out as app. 2 m × 1 m size block in thickets of dwarf pine in part of the main ridge of the Low Tatra Mts. between Ďurková and Zámostská Hoľa summits. The leucogranite body is emplaced within deformed and altered porphyritic Bt granodiorites–granites of Prašivá type (Fig. 1C). The border between the hosting Bt-granodiorite and the leucogranite body is sharp. The ZHG dyke is located close to tens of metres wide quartz–K-feldspar–muscovite pegmatite veins. The whole studied area is extensively deformed: the major fault system has S–E and NNW–SSE directions, and is related to the Alpine imprint, whereas E–W and NW–SE systems are considered to be pre-Alpine (Sasvári &Rozložník 1993).

The LTP belongs to the principal ore district within the TS and CWC in general and includes tens of polymetallic deposits developed during several mineralization stages from Carboniferous to Paleogene (Chovan et al. 1996; Majzlan et al. 2020a, b and references therein). The studied area is located close to the Magurka polymetallic Au–Sb–W deposit (Fig. 1C), which forms a tectonically-controlled, parallel vein system of mostly E–W direction and dipping towards the S in Prašivá granitic rocks (see fig.1 in Chovan et al. 1995).

Methods

The methodology included whole rock major and trace elements analysis (ACME, Canada), petrographic and microtextural description under optical microscope, back-scattered electron imaging (BSEI), WDS (wavelength dispersive spectrometry) electron microprobe analysis of mineral phases (EMPA) all performed at the Earth Science Institute in Banská Bystrica and monazite U–Th–total Pb microprobe dating realized at Dionýz Štúr State Geological Institute. The representative rock sample ~2 kg was taken during field works in summer 2019. The polished thin sections of the rock were used for petrographic and microtextural studies. One hand-specimen size sample was crushed, ground, and pulverized. Whole-rock analyses was performed at the Bureau Veritas by ICP-MS lithium borate fusion.

Back-scatter electron imaging (BSE) and determination of mineral chemistry via wavelength-dispersive spectrometry (WDS) were performed on a JEOL JXA 8530FE electron probe microanalyser (EMPA) at the Earth Sciences Institute of Slovak Academy of Sciences in Banská Bystrica, Slovak Republic.

Silicate minerals (biotite, feldspars) were analysed using a 15.0 kV accelerating voltage and 17 nA beam current.

Standards for the silicate minerals are Ca(Kα)-diopside, K(Kα)-orthoclase, Na(Kα)-albite, Mn(Kα)-rhodonite, Mg(Kα) (albite)-diopside, Mg(Kα) (micas and chlorite)-biotite, Si(Kα) (micas and chlorite)-biotite, Si(Kα) (albite)-orthoclase, Al(Kα) (micas)-orthoclase, Al(Kα) (albite)-albite, Zn(Kα)-gahnite, Ni(Kα)-nickel silicide, Cr(Kα)-Cr2O3, Fe(Kα)-hematite, P(Kα)-apatite Sr (Lα)-celestite, Ba(Lα)-barite, Cl (Kα)-tugtupite, F(Kα)-fluorite, and Ti(Kα)-rutile.

Zircon, thorite, monazite, allanite and xenotime were analysed using a 15 kV accelerating voltage and a beam current of 20 nA. Counting times for Th, U, and Pb were 30 s on peak and 15s on background, and for REE 20 s on peak and 10 s on background. The beam diameter varied from 2 to 7 μm depending on the grain size. EPMA data was reduced using the ZAF correction method. Standards for the REE-bearing minerals included: Ca (Kα)-diopside, apatite, F (Kα)-fluorite, Cl (Kα)-tugtupite, Na (Kα)-albite, Sr (Lα)-celestite, Si (Kα, TAP)-albite, Al (Kα)-albite, Mg (Kα)-diopside, K (Kα)-orthoclase, P (Kα)-apatite, $CePO_4$ (in monacite), U (Mβ)-UO_2, Th (Mα)-thorianite, Pb (Mβ)-crocoite, Y-(Lα)-YPO_4, Lu (Lα)-$LuPO_4$, Ho (Lβ)-$HoPO_4$, Yb (Lα)-$YbPO_4$, Tm (Lα)-TmPO4, Er (Lα)-ErPO4, Gd (Lβ)-GdPO4, Dy (Lα)-DyPO4, Tb (Lα)-$TbPO_4$, Sm (Lβ)-$SmPO_4$, Eu (Lα, LIFH)-EuPO4, Pr (Lβ)-PrPO4, Nd (Lα)-NdPO4, Ce (Lα)-CePO4, La (Lα)-LaPO4, Ta (Mα)-$CrTa_2O_6$, Nb (Lα)-$LiNbO_3$, Hf (Mα)-cubic zirconia, Zr (Lα)-cubic zirconia, Zn (Kα)-willemite, Fe (Kα)-hematite, Mn (Kα)-rhodonite, Cr (Kα)-Cr_2O_3, V (Kα)-vanadinite, Ti (Kα)-rutile, Ba (Lα)-barite, Sc (Kα)-$ScVO_4$, Nb (Lα)-$LiNbO_3$, As(Lα)- gallium arsenide, W (Lα)-scheelite. Corrections of line interferences of Nd→Ce, Eu→Nd, Pr, Gd→Ho, Tm→Sm, Nd→Ce Lu→Dy, Lu→Ho, U→Th, K, V→Ti, were provided by Amli & Griffin's (1975) method.

Monazite age testing was carried out by an electron microprobe CAMECA SX 100 housed in the State Geological Institute of Dionýz Štúr in Bratislava (Slovak Republic). The main principles of the dating procedure were published by Konečný et al. (2018), however, succeeding improvements that were recently added have not been published yet. The measuring conditions (15 kV accelerating voltage and 180 nA beam current, 3 μm beam current) remained the same. A complete analysis was acquired, including REEs, As, Sr, S, Si. Long counting times for elements critical to dating were implemented, for example, 300 s on PbMα (LPET), 80 s on UMβ, 35 s on ThMα, and the same time in the background. Cerrusite, uraninite, and thorianite were used for calibration of Pb, U, and Th. The non-linear background height at PbMα position due to distant background points was estimated using an original method described in this paper (function of curvature to mean atomic number). Numerous peak interferences were corrected via ZAF implemented empirical procedure. The most important were PbMα overlapped by ThMζ1, ThMζ2 and YLγ2,3, UMβ overlapped by multiple ThMζ, ThM3-N4 and ThM5-P3 lines and other interferences among REE's listed in this paper. Detailed examination revealed interference of combined UMζ1 and UMζ2 peaks, which have a distant tail interfering with the PbMα background point at a relative position of $-3255\ \sin\theta*10^{-5}$ (CAMECA R=160 Rowland circle) from the peak position. The other interference at the same background point comes from weak self-interference of PbM4-O2. Both interferences compromising background at PbMα ($-3255\ \sin\theta*10^{-5}$) were carefully measured and removed. To prove that the microprobe is capable of producing reliable ages, a procedure called MARC (monazite age reference calibration) may indicate and suppress any unwanted systematic errors which may degrade the dating accuracy regardless of the number of analyses accumulated. Fine tuning by calibration lines derived from measurements on monazites (ΔPb vs. Th and ΔPb vs. Y where ΔPb is deviation from the reference age) with well-constrained ages by SIMS, TIMS, SHRIMP, etc. improves reliability of dating. Calibration lines are constructed by using 5 age monazite reference materials (ARM's). With an increasing number of reference monazites, the confidence in age estimation grows, while the lines are better constrained. Using high beam currents causes "beam damage" at the analysis spot and is the reason for beam current instability. A time dependent correction procedure was applied to re-adjust correct counting ratios between Th–U–Pb and Y (the last because of interference with PbMα).

Results

Petrography and whole-rock chemistry of ZHG

The ZHG is fine-grained, pale-pinkish to pale-grey granite (Fig. 2A); it consists of K-feldspar, plagioclase, quartz and muscovite in modal proportions corresponding to quartz-rich syenogranite-granite. The ZHG is characterized by a highly heterogeneous grain size microtexture, manifested by three generations of rock-forming minerals: (1) subhedral to anhedral, varying in size 1–4 mm phenocrysts of plagioclase, K-feldspar, quartz and rare chlorite and muscovite; (2) fine-grained (<0.5 mm in diameter) K-feldspar, quartz and muscovite, with rare plagioclase and chlorite forming interstitial channels; (3) large, late quartz and muscovite, which fill fractures in the rock, and replace disrupted K-feldspar phenocrysts.

The representative EPMA analyses of rock-forming minerals are listed in Supplementary material S1. Phenocrystic plagioclase forms euhedral, prismatic grains (Fig. 2B, D), whereas matrix plagioclase is sub- to anhedral and only rarely euhedral (Fig. 2C). Both textural types show strongly lobate grain boundaries on contact with K-feldspar (Fig. 2C, D), and frequently enclose rounded quartz droplets. Regardless of size and textural position, plagioclase is normal, or weakly oscillatory zoned in cores, whereas rims show patchy zonation; phenocrystic plagioclase varies from core 20–17 to rim 10–2 mol% of X_{An}. Matrix plagioclase is generally lower in An (X_{An} 12–2 mol%). Phenocrystic K-feldspar forms subhedral, brittle deformed grains (Fig. 2E), whereas one in a matrix is anhedral (Fig. 2C). Matrix plagioclase and K-feldspar contain up to 0.3 wt% P_2O_5, whereas the phenocrystic feldspars

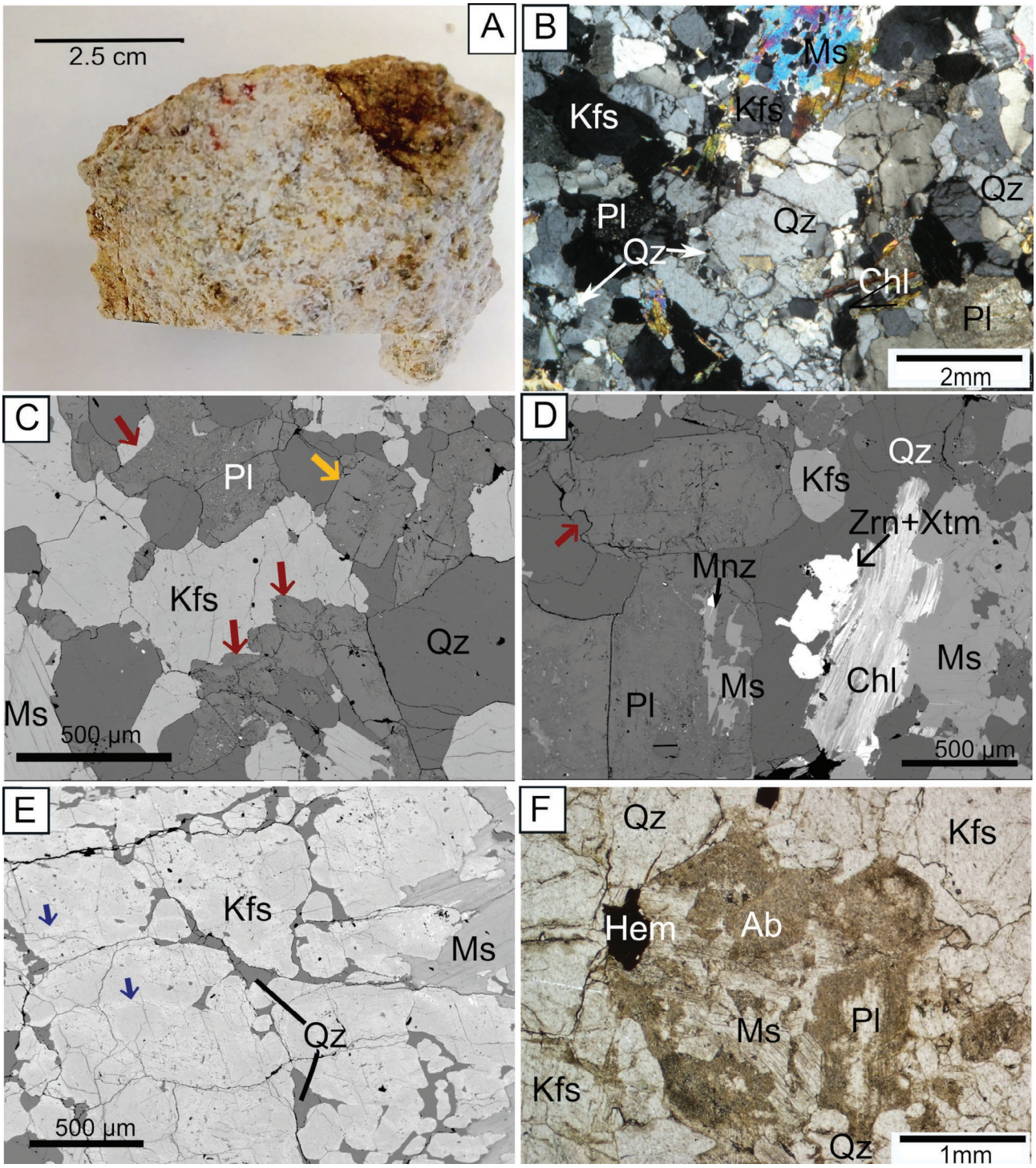

Fig. 2. A — the ZHG in hand specimen. **B–E** — Microtextures of ZHG: **B** — Brittle fractured plagioclase, quartz and K-feldspar surrounded by fine-grained "matrix" of quartz, K-feldspar and plagioclase; late muscovite and quartz have crystallized within fractures. **C** — "Matrix" assemblage; note strongly embayed, reactive boundaries of plagioclase (brown arrows) and its locally preserved euhedral shape (yellow arrow) and the presence of polygonal aggregates of K-feldspar and quartz. **D** — Euhedral plagioclase phenocrysts surrounded by quartz; muscovite takes the form of platy crystals instead of fine-crystalline, "sericite" inside altered plagioclase. The plagioclase–quartz boundary is predominantly straight but local embayments occur (red arrow). **E** — Disintegrated K-feldspar phenocryst filled by quartz and muscovite; note dendritic net of brighter channels (blue arrows), which are enriched in P and Ab. **F** — Extensive replacement of plagioclase phenocryst by platy muscovite and albite. Abbreviations: Pl – plagioclase, Ms – muscovite, Qz – quartz, Kfs – K-feldspar, Chl – chlorite, Zrn – zircon, Xtm – xenotime, Hem – hematite, Ab – albite.

are usually lower in P_2O_5 (<0.1 wt%), although grain rims and secondary veinlets are exceptions (Fig. 2E). Phengitic muscovite forms fibrous, needle-like aggregates with chlorite and iron oxides, and minute laths within matrix; late muscovite is up to 5 mm in size, and encloses resorbed K-feldspar and plagioclase (Fig. 2D). Phenocrystic quartz forms oval or strongly irregular, brittle-deformed grains with locally straight, recrystallized grain boundaries, whereas matrix quartz is interstitial between feldspars and shows sutured grain boundaries (Fig. 2C). Late quartz fills interstitial spaces between phenocrysts (Fig. 2D) and fissures in brecciated phenocrysts (Fig. 2E). The mineral alteration is widespread, especially in the phenocrysts generation, and includes extensive replacement of plagioclase by albite and muscovite (Fig. 2D, F), and presence of muscovite, chlorite and Fe oxides aggregates, representing products of total decomposition of a biotite. The accessory mineral assemblage in the ZHG is represented by zircon, xenotime-(Y), monazite-(Ce), allanite-(Ce) and rare apatite; details see in the Results section.

Geochemical data (Supplementary Material S2) shows that the ZHG is silica-rich (>74 wt% SiO_2) peraluminous granite (ASI=1.23), elevated in alkalis, potassic ($K_2O/Na_2O>2$), and low in CaO (0.58 wt%), FeO_t (1 wt%), MgO (0.24 wt%) and TiO_2 (0.09 wt%), and extremely depleted in P_2O_5 (<0.1 wt%; Fig 3A). The ZHG is significantly lower in Sr (130 ppm) and higher in Rb (141 ppm) than the host Prašivá granodiorites (600–1200 and 80–120 ppm, respectively; Maraszewska et al. 2022), but relatively high in Ba (>400 ppm), and is low in V, Co, Zr and Ni content and Nb/Ta (wt%) ratio (~5). The ZHG is high in Y (28 ppm) and very low in total REE content (57 ppm), and its chondrite-normalized REE pattern is strongly asymmetric, with enrichment in MREE and HREE (La/Yb~2), and contrasts with high REE's content (100–300 ppm) and LREE-enriched pattern (La/Yb: 20–80) of the host granodiorite, but also the other, less HREE-enriched leucogranites in the LTP (Fig. 3B). Low contents of ΣREE and Zr are consistent with very low Zr saturation temperatures (~650 °C Boehnke et al. 2013) and moderate REE saturation temperatures (~720 °C; Montel 1993).

Microtextures and chemistry of the accessory minerals

Zircon

Zircon in the ZHG is mostly hosted by matrix feldspars or is interstitial (Fig. 2D). Zircon crystals are commonly disrupted into smaller, angular or rounded fragments, which are inter- or overgrown, by xenotime-Y (Fig. 4A, B, D–F). Zircon ranges from 10 to 200 μm in size, and in most of the grains, the prismatic, bipyramidal outline is partially retained (Fig. 4A) but disturbed to varying extents by embayments of crystal faces and rounding of the prisms (Fig. 4B–F), leading locally to ameboidal (Fig. 4B) or relict (Fig. 4E, F) forms. Some euhedral and subhedral grains display truncated concentric, oscillatory zonation (Fig. 4A), but most of the grains are patchy zoned (Fig. 4B), or homogeneous in BSEI (Figs. 4 D–F). The different zonation styles can overlap in a single grain (Fig. 4C). Most of the euhedral, zoned grains are cut by system of fissures, characteristic of metamict zircon (Fig. 4A). Irregular crystals show pronounced microporosity (Fig. 4A, C). On the basis of microtexture, zircon was subdivided into two groups: the first zircon group (Zrn1) refers to apparently igneous zircon, while the second group of zircon (Zrn2) represents altered, or recrystallized zircon (see details in Discussion).

The representative WDS analyses of the ZHG zircon are listed in Supplementary material S3. Zircon shows variable enrichment in HfO_2 (1.8–3.2 wt%; 0.017–0.029 apfu) and low Zr/Hf (wt%) ratios 14.6–23.9; Fig. 5A). HfO_2 content and Zr/Hf ratio in Zrn1 and Zrn2 largely overlap, but HfO_2 >3.0 wt% is found exclusively in the most resorbed Zrn2 grains. Zircon in the ZHG is depleted in Zr and Si (Zr+Si 1.71–1.96 apfu), which is related to non-essential structural components (NESC; Fig. 5B) observed mainly in the apparently primary Zrn1 grains, where it is reflected in concentric zonation. In Zrn2, the content of NESC is related to the extent of the alteration and recrystallization – in less altered or brighter

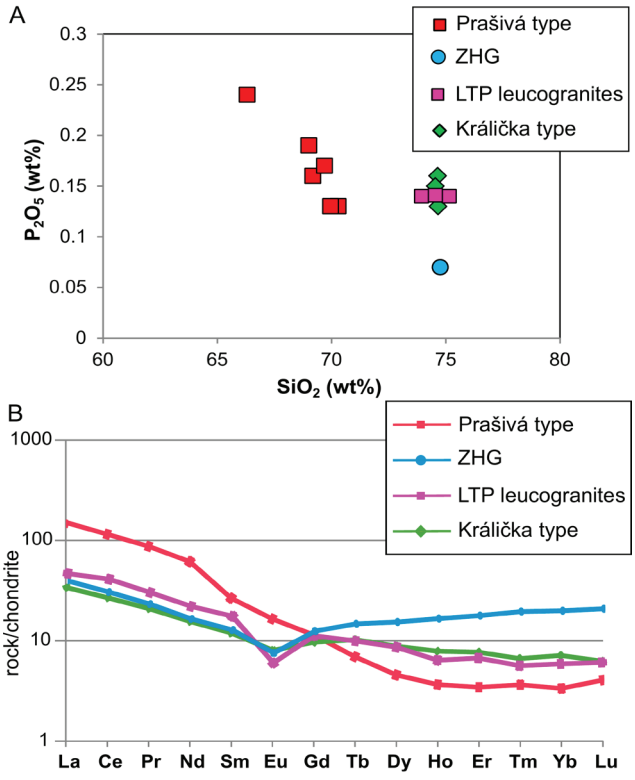

Fig. 3. A — Chondrite-normalized REE pattern of Zámostská Hoľa leucogranite (ZHG) compared to representative patterns of hosting granodiorite (from Maraszewska et al. 2022), other leucogranite bodies in the LTP, Králička muscovite leucogranite (Maraszewska, unpublished data). Normalization values after McDonough and Sun (1995). **B** — Whole-rock P_2O_5 vs SiO_2 relations in different types of granites in the LTP (data from Maraszewska et al. 2022; Maraszewska, unpublished data).

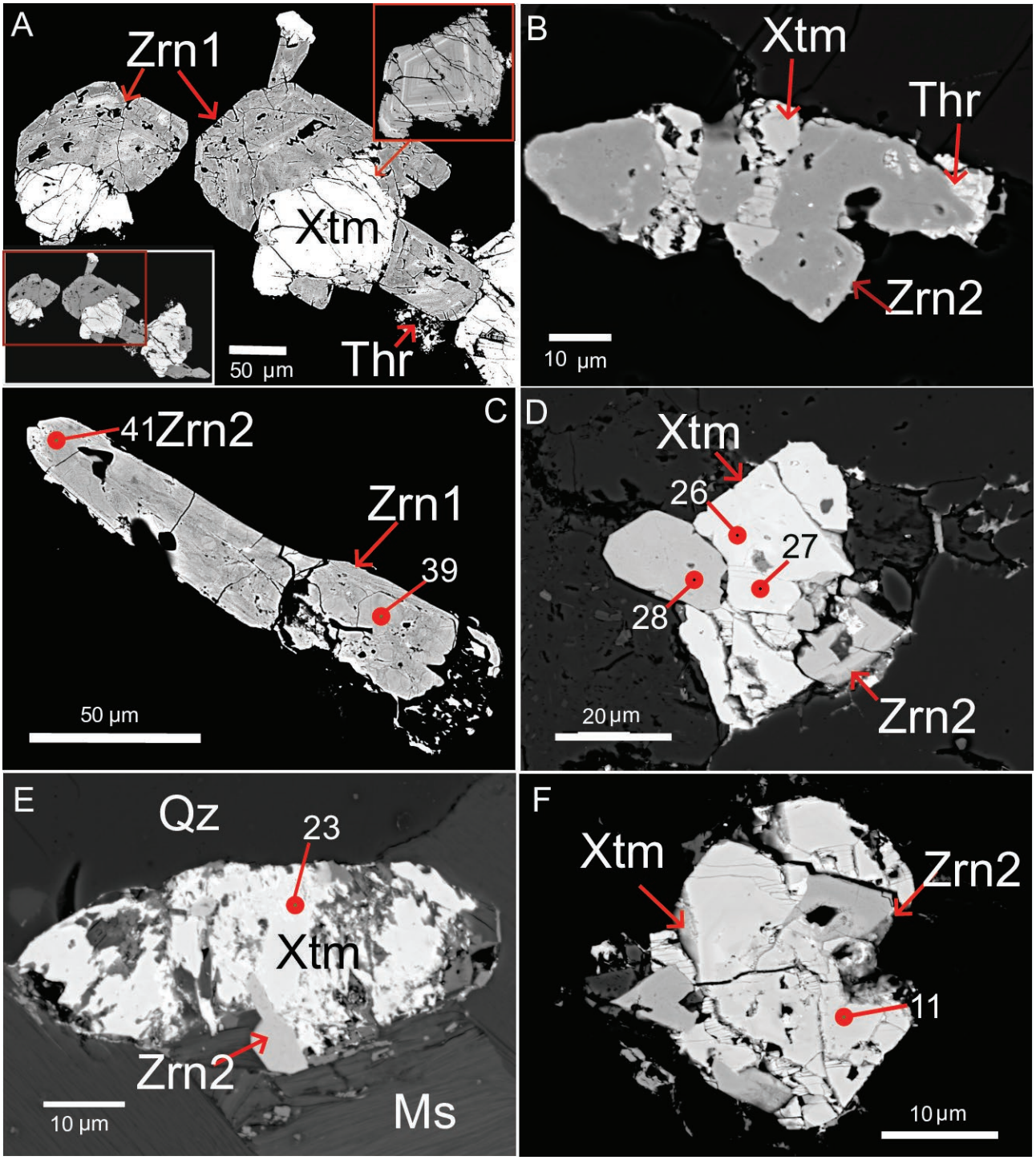

Fig. 4. Zircon (Zrn) and xenotime (Xtm) microtextures in the ZHG. **A** — Cluster of disrupted, euhedral, metamict Zrn1 intergrown with euhedral, regularly zoned xenotime – note small aggregates of thorite (Thr) on zircon rims. **B** — Unzoned Zrn2 with blurred, irregular grain boundary and anhedral xenotime growing epitaxially within fissures in zircon; bright inclusions and overgrowths are compositionally close to thorite (Thr). **C** — Zrn2 exhibiting preserved elonged outline, disturbed by strongly resorbed, locally skeletal grain boundary, with remnants of convolute oscillatory zonation within apparently homogeneous or patchy-zoned, microporous domains. **D** — Subhedral, patchy zoned xenotime enclosing strongly resorbed, unzoned Zrn2; the boundary between the phases is highly reactive and diffusive. **E** — Skeletal, strongly heterogeneous xenotime aggregates forming pseudomorphose after zircon, which survived as a tiny relict. **F** — Angular relicts of disrupted zircon enclosed within strongly irregular, epitaxial xenotime: note the diffusive character of the zircon-xenotime boundary and the overall look that zircon has been torn apart by growing xenotime. Numbers refer to spot analysis of zircon and xenotime listed in Supplementary materials S3 and S4, respectively.

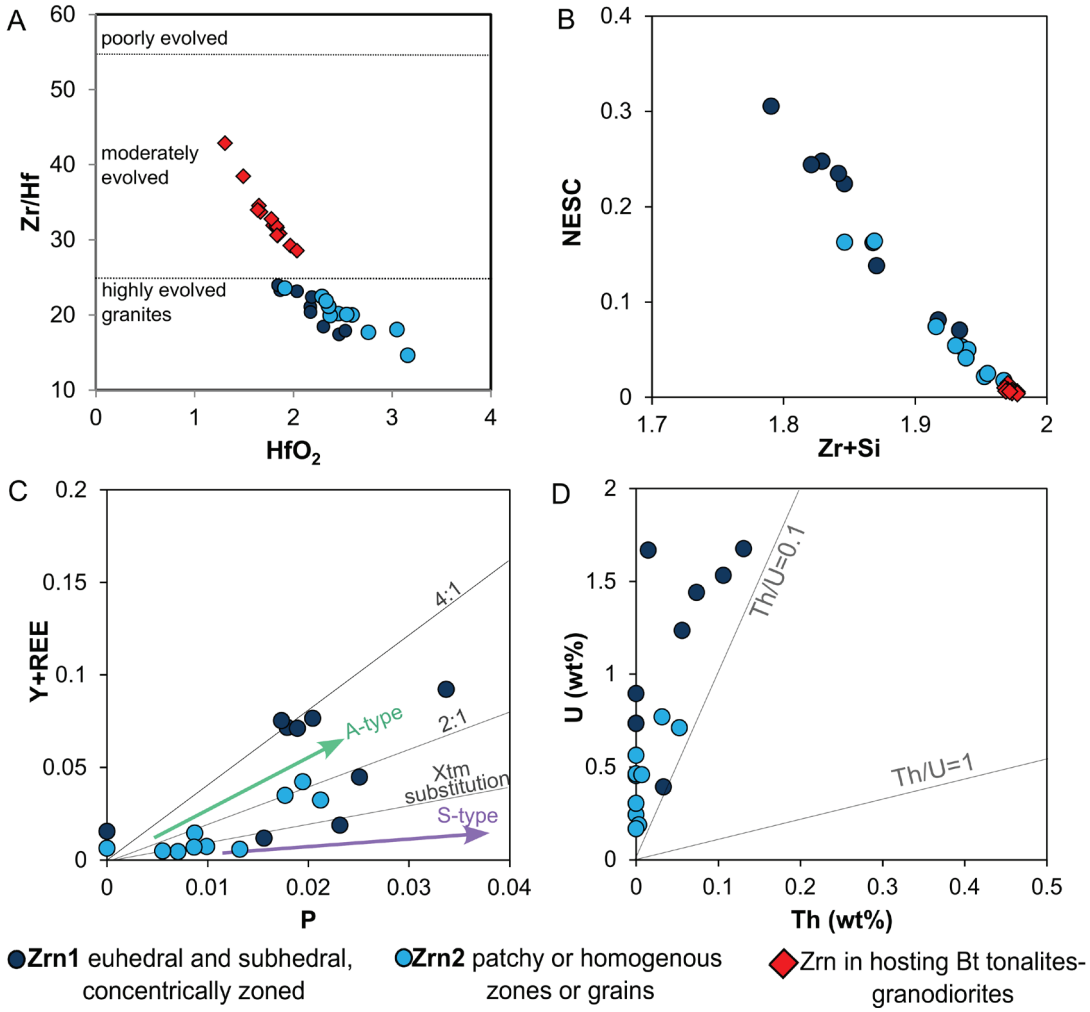

Fig. 5. Compositional variations of the ZHG zircon. **A** — HfO_2 vs Zr/Hf (wt%) plot with Zr/Hf ratios typical for poorly, moderately and highly evolved granitoids defined by Breiter et al. (2014). **B** — NESC vs Zr+Si (apfu) showing enrichment in NESC (U, Th, REE, Fe, Ca, Al, Sc, As, P) coupled with depletion in Zr and Si. **C** — Y+REE vs P (apfu) with trends of zircon in evolved A and S type suites (after Breiter et al. 2014; René 2014). **D** — U vs Th (wt%) relations in zircon.

domains in patchy zoned grains, it is roughly similar to Zrn1, whereas anhedral and homogeneous grains are closer to ideal $ZrSiO_4$.

Zrn1 and brighter patches in Zrn2 are high in P_2O_5 (up to 1.19 wt% and 0.033 apfu), Y_2O_3 (up to 3.9 wt% and 0.07 apfu) and HREE ($\Sigma(Gd–Lu)_2O_3$ up to 2 wt% and 0.021 apfu). The Y+REE's and P show a positive relationship, but it deviates from the ideal xenotime-type substitution trend $(Y+REE)^{3+}+P^{5+} \leftrightarrow 2\ Zr^{4+}$; Förster 2006; Fig. 5C), which suggests a more complex mechanism of REE's incorporation. UO_2 varies in the range of 0.27–1.9 wt% (0.001–0.014 apfu) and is remarkably higher in Zrn1 than in Zrn2, whereas ThO_2 is very low in the both types (b.d.l.–0.15 wt%; 0.000–0.002 apfu), resulting in very low Th/U (wt%) ratio (0.0–0.4; Fig. 5D). The contents of other NESC (CaO, FeO, Al_2O_3) are strongly variable (each from <0.2 to 0.8–1.3 wt%) and increase with P, Y+REE, and U contents (not shown). The As_2O_5 content is highly scattered (b.d.l.–0.5 wt%) in both types, and is the highest in patchy zoned and Y+REE undepleted Zrn2. Both Zrn1 and Zrn2 contain variable amounts of F (b.d.l.–0.15 wt%) and Cl (b.d.l.–0.19 wt%). The low analytical totals (93–96 wt%) are characteristic especially for Zrn1.

Thorite forms grains and aggregates on the rims of Zrn1 (Fig. 4A), whereas in Zrn2, it also occurs as inclusions (Fig. 4B). Thorite is relatively high in UO_2 (4.9 wt%) and $Y+REE_2O_3$ (7.5 wt%), suggesting coffinite-xenotime-thorite solid-solution, and shows low analytical totals (Supplementary material S3).

Xenotime-(Y)

Xenotime-(Y) in the ZHG (abbreviated further in text to xenotime) directly coexists with zircon as over- and intergrowths on zircon fragments (Fig. 4A–C, E). Some aggregates remind pseudomorphoses after zircon (Fig. 4D). Xenotime shows a wide range of microtextures; large (up to 300 μm),

euhedral crystals are exceptional (Fig. 4A), and most of the grains vary 100–10 μm size and are subhedral to strongly anhedral, or form grainy aggregates with blurred boundaries (Fig. 4B, D–E). Some euhedral crystals show clearly-visible concentric, oscillatory zoning (Fig. 4F); however, most of the xenotime is irregularly zoned or unzoned. The contact between zircon and xenotime varies from sharp to strongly diffusive.

Representative analyses of xenotime are listed in Supplementary material S4. Xenotime shows a wide range of concentrations of UO_2 (0.3–3.2 wt%; 0.002–0.024 apfu) and ThO_2 (<0.1–1.2 wt%; <0.001–0.01 apfu; Fig. 6A) and low Th/U ratio 0.1–0.6; Fig. 6B). The larger, euhedral or subhedral grains contain highest amounts of U, and lowest Th/U, whereas lowest U and highest Th/U were constrained in small irregular grains. The coffinite/thorite-type substitution generally predominates (Fig. 6C) but the cheralite component increases in some irregular grains. Xenotime contains 38–45 wt% (0.69–0.785 apfu) of Y_2O_3 and 17–22 wt% (0.193–0.250 apfu) of ΣREE_2O_3, and is relatively low in the LREE's, with a variably marked hump on MREE and Lu in REE patterns (Fig. 6D). The Y/Dy and Gd/Yb ratios are strongly variable and range from "magmatic/primary" to "secondary/hydrothermal" xenotime ratios (Fig. 6E). As_2O_5 ranges b.d.l.–2.3 wt% and 0.00–0.052 apfu pointing to varying contents of chernovite molecule (Y,HREE(AsO_4); Fig. 6F) and it is the highest in strongly irregular aggregates; F content in xenotime is <0.2 wt%.

Monazite-(Ce)

Monazite-(Ce) in the ZHG (abbreviated further in text to "monazite") is modally less abundant than xenotime. It forms inclusions in phenocrysts of feldspars or within muscovite–chlorite aggregates. Typical size of the monazite ranges from 50 to 120 μm in diameter. Despite the variable degree of corrosion of the grains, a primary tabular shape is preserved, as well as regular or sector zoning in cores (Fig. 7A, B). The outermost rim zones are sutured and distinctively brighter in the BSEI compared to the cores (Fig. 7B, C); the patchy zonation and microporosity is observed in some grains as well (Fig. 7C). Texturally, two types of monazite have been distinguished. Monazite of the first type (Mnz1) represents the primary form; while monazite of the second type (Mnz2) represents the alteration zones on monazite rims and the irregular patches.

The representative analyses of the monazite are listed in Supplementary material S4. Both Mnz1 and Mnz2 are relatively high in ThO_2 (4.0–9.5 wt%; 0.034–0.082 apfu) but strongly differ in U content (Fig. 6A) and Th/U ratio (Fig. 6B). Mnz1 is usually higher in UO_2 (up to 1 wt%), and lower in Th/U (wt%) ratio (4–12) than Mnz2 (UO_2<0.5 wt% and Th/U 24–103). The Th/U ratio is strongly positively related to Si/Ca ratio (Fig. 6B); in Mnz1, cheralite substitution predominates (Fig. 6C), whereas Mnz2 shows an increase of huttonite molecule (Fig. 6C). The REE patterns of Mnz1 and Mnz2 are relatively coherent, and gently incline from Gd to Yb (Fig. 6D). The Y_2O_3 content in monazite is in the range of 0.8–3.2 wt% and 0.017–0.063 apfu, and is higher in Mnz1, than coexisted in the same grain zones of Mnz2. Application of monazite–xenotime geothermometry (acc. to Pyle et al. 2001) yielded a slightly higher temperature range in Mnz1 (520–610 °C) than in Mnz2 (370–510 °C). TheAs_2O_5 content is low in both Mnz1 and Mnz2 (<0.19 wt%; Fig. 6F), but both contain up to 0.85 wt% and 0.1 apfu of F.

Allanite-(Ce)

Allanite-(Ce) (abbreviated later in the text to "allanite") is a rare mineral in the ZHG; it occurs as a net of thin dendritic veinlets developed in the K-feldspar or plagioclase (Fig. 8A) and only locally forms larger accumulations up to 100 μm size, which fill the cavities in hosting feldspars (Fig. 8B). In the larger accumulations of allanite, the inner zones are brighter in BSEI than the external ones but the transition is strongly diffuse, excluding typical magmatic zonation (Fig. 8B); nevertheless, most common is irregular zonation (Fig. 8C).

Representative analyses of allanite are listed in Supplementary material S5. Allanite in the ZHG shows relatively uniform contents of Al_2O_3 (17.7–20.3 wt% and 1.98–2.20 apfu), CaO (11–13.8 wt% and 1.11–1.36 apfu), and FeO content (FeO_t 10.2–11.5 wt%; 0.79–0.92 apfu; Fe^{3+}/Fe_{tot} (apfu) 0.24–0.4). According to REE+Y+U+Th vs Al_{total} relations (Fig. 9A), allanite occupies a transitional position from the field of peraluminous granites to the field of secondary allanite. The allanite is elevated in MnO (1.4–2.3 wt%; 0.11–0.18 apfu) and Y_2O_3 (≤1.6 wt% and 0.08 apfu). The total content of REE_2O_3 varies from 12.7 to 20.2 wt%, and the REE patterns are flat and MREE/LREE enriched in comparison with the orthomagmatic allanite in the granodiorite (Fig. 9B) and La/Nd and (La+Nd+Pr)/ΣREE (atomic%) range between granite's and pegmatite's allanite averages (Fig. 9C). The allanite is very low in ThO_2 and UO_2 (both <0.15 wt%) and shows low Th/U(wt%) ratio (<4.0). F in allanite is up to 0.2 wt%.

Apatite

Apatite in the ZHG usually forms very small (10–30 μm) inclusions in plagioclase and K-feldspar (Fig. 8D) and is anhedral without detectable microtextural or compositional zoning. Apatite represents almost pure fluorapatite end-member with low Y+REE_2O_3 (0.15–0.2 wt%), MnO (<0.25 wt%), and FeO (<0.1 wt%; Supplementary material S6).

Monazite U–Th–Pb geochronology

The average U–Th–total Pb monazite age is 345±2.5 Ma (Fig. 10; Supplementary material S7); the datings were performed on the unaltered cores of Mnz1 type. The spot datings range from 330 to 379 Ma; the individual apparent age domains, often varying 30 Myr, often coexist in single grains

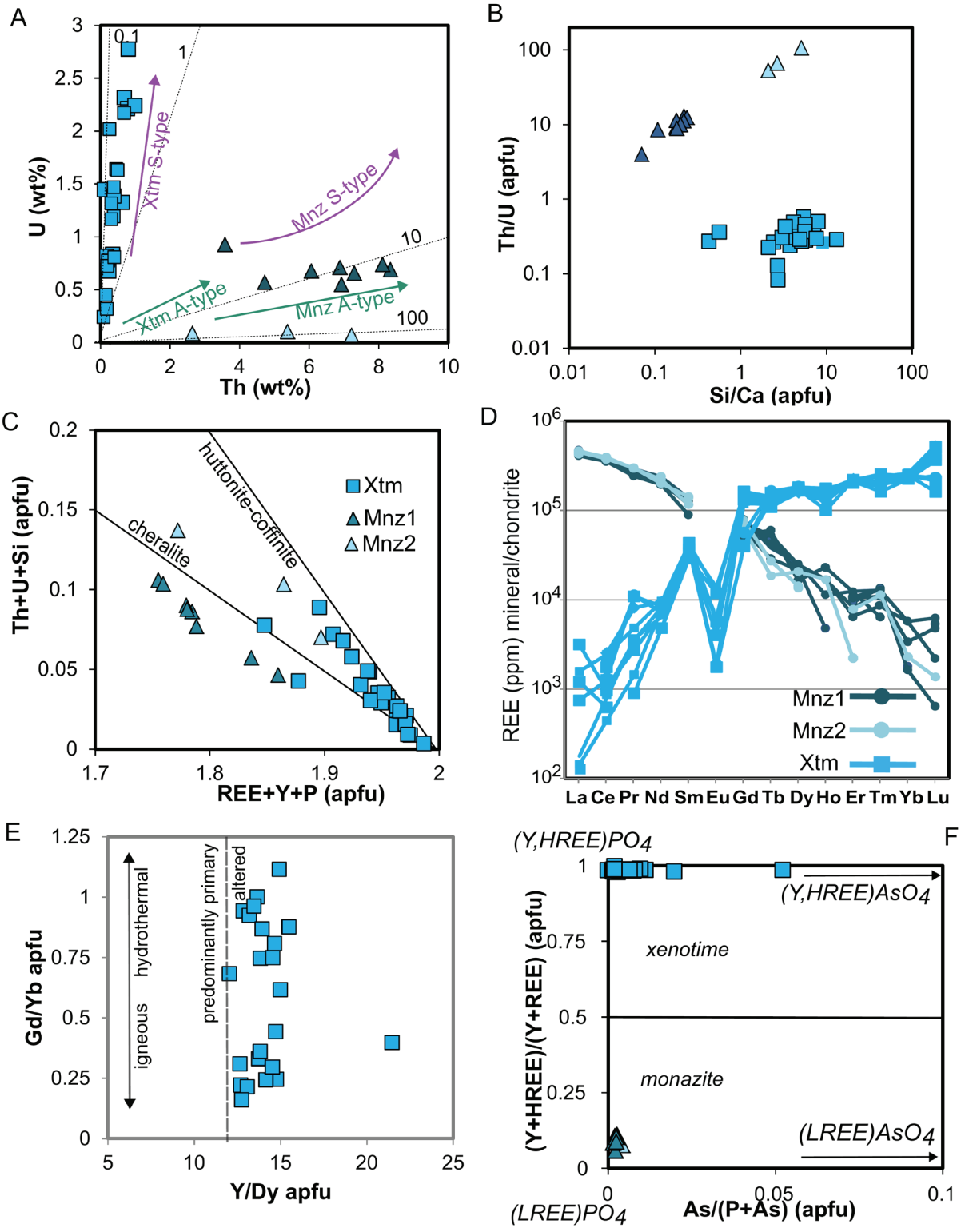

Fig. 6. Compositional variations of xenotime and monazite in the ZHG. **A** — U vs Th relations in xenotime and monazite; trends in S and A type granites acc. to Förster (1998a,b) and Breiter & Förster (2021); **B** — Th/U vs Si/Ca (apfu) plot showing different mechanism of U and Th incorporation pronounced in Mnz1 and Mnz2; **C** — Th+U+Si(apfu) vs REE+Y+P (apfu) plot with vectors of huttonite/coffinite–thorite and cheralite-type substitutions; **D** — Chondrite-normalized REE (in ppm) plot of xenotime and monazite; normalization values after McDonough & Sun (1995); **E** — Gd/Yb vs Y/Dy(wt%) plot: distinction of igneous and hydrothermal xenotime by Gd/Yb modified after Kositcin et al. (2003); border subdividing primary, low Y/Dy, and altered, high Y/Dy xenotime after Breiter et al. (2009); **F** — chernovite and gasparite substitution mechanisms in xenotime and monazite; after Ondrejka et al. (2007), modified.

and show no clear relation with the zoning and chemical composition (as contents of Y, U or other elements).

Discussion

Magmatic versus secondary origin of zircon in the ZHG

The early-crystallized, orthomagmatic zircon is, in general, euhedral, and regular concentric zoned (Corfu et al. 2003); the ZHG zircon shows much more diversified microtextures, expressed by a variety of grain morphology and zonation styles (Fig. 4). The very fine, convolute, oscillatory zonation displayed by Zrn1 (Fig. 4A) recalls late-crystallized zircon in highly differentiated granites and aplites (Hoskin & Ireland 2000; Corfu et al. 2003; Erdmann et al. 2012); on the other hand, the microtextures of Zrn2 such as embayment of crystal boundaries (Fig. 4B–E) leading to the relict character (Fig. 4D, E); microporosity; irregular zonation, or, in opposite, apparent homogeneity; are evidence of dissolution–reprecipitation process via zircon-fluid (Geisler et al. 2007; Erdmann et al. 2012; Harlov et al. 2023) or zircon-melt interaction (Gagnevin et al. 2010). The radiant or concentric fracturing observed in Zrn1 is typical for metamict zircon (Corfu et al. 2003), whereas the disruption and dislocation of the fragments (occurring in both Zrn1 and Zrn2), likely result from its brittle deformation coeval with the phenocrysts of rock-forming minerals during subsolidus brecciation, and/or expansive growth of associated xenotime.

The microtextural complexity of the zircon in ZHG is reflected in the diversified chemistry. Typically, pristine igneous zircon in hosting Prašivá type granodiorite, but also in general in the Variscan granitoids in TS contains low amounts of NESC as P, Y, HREE, As, and others, and shows Th/U(wt%)>0.5 and Zr/Hf(wt%) ~30–65 and 1.2–2.1 wt% of HfO_2 (Poller et al. 2001; Broska et al. 2012; Maraszewska, unpublished data). The low Zr/Hf(wt%)<24 (Fig. 5A) and Th/U(wt%)<0.4 (Fig. 5D), as well as enrichment in NESC (Supplementary material S3; Fig. 5B) in the ZHG zircon reminds either ones in most fractionated lithofacies of peraluminous granitic suites, or pegmatite systems (Pérez-Soba et al. 2007; van Lichtervelde et al. 2009; Breiter et al. 2014; René 2014; Mahdy 2021). The origin of such an exceptional signature can be dual. An enrichment in NESC and lowering of Zr/Hf and Th/U are documented in zircon, which was metasomatized by hydrothermal fluids (Geisler et al. 2007; Breiter et al. 2014; Kelly et al. 2020). However, in the case of zircon in the ZHG, the igneous origin of NESC enrichment is supported by their higher concentrations in most euhedral and apparently earlier Zrn1 than coexisting secondary domains of Zrn2. Together with the microtextures typical for late-stage zircon, it implies crystallization from low Zr/Hf, and high U/Th and Y+HREE fluid-rich, evolved magma (Pérez-Soba et al. 2007; van Lichtervelde et al. 2009; Mahdy 2021), or a reequilibration of the entire crystals by such melt during late-stage, but still magmatic processes

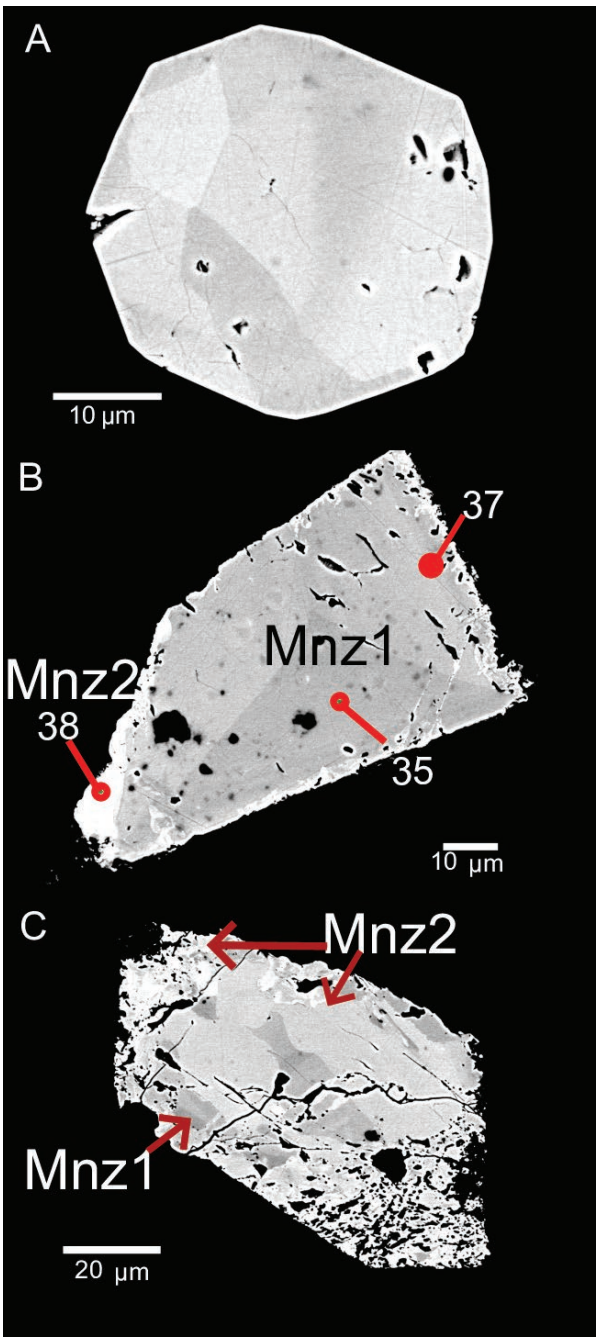

Fig. 7. BSE images of monazite microtextures. **A** — Euhedral, weakly sector-zoned monazite; note locally developed microporosity. **B** — Subhedral monazite with strongly corroded grain boundaries, composed of sector-zoned Mnz1 and distinctively brighter irregular rim of Mnz2. **C** — Sieve-like monazite grain with preserved euhedral outline; homogeneous, patchy zones of Mnz2 transgressively overprint Mnz1. Numbers refer to spot analysis of monazite listed in Supplementary material S4.

(Park et al. 2016). The second possibility can be supported by secondary U- and Y-rich thorite inclusions and rim grains resulting from expelling of Th from metastable zircon structure (Pointer et al. 1988); nevertheless, the textural and compositional distinction between the late-stage igneous and

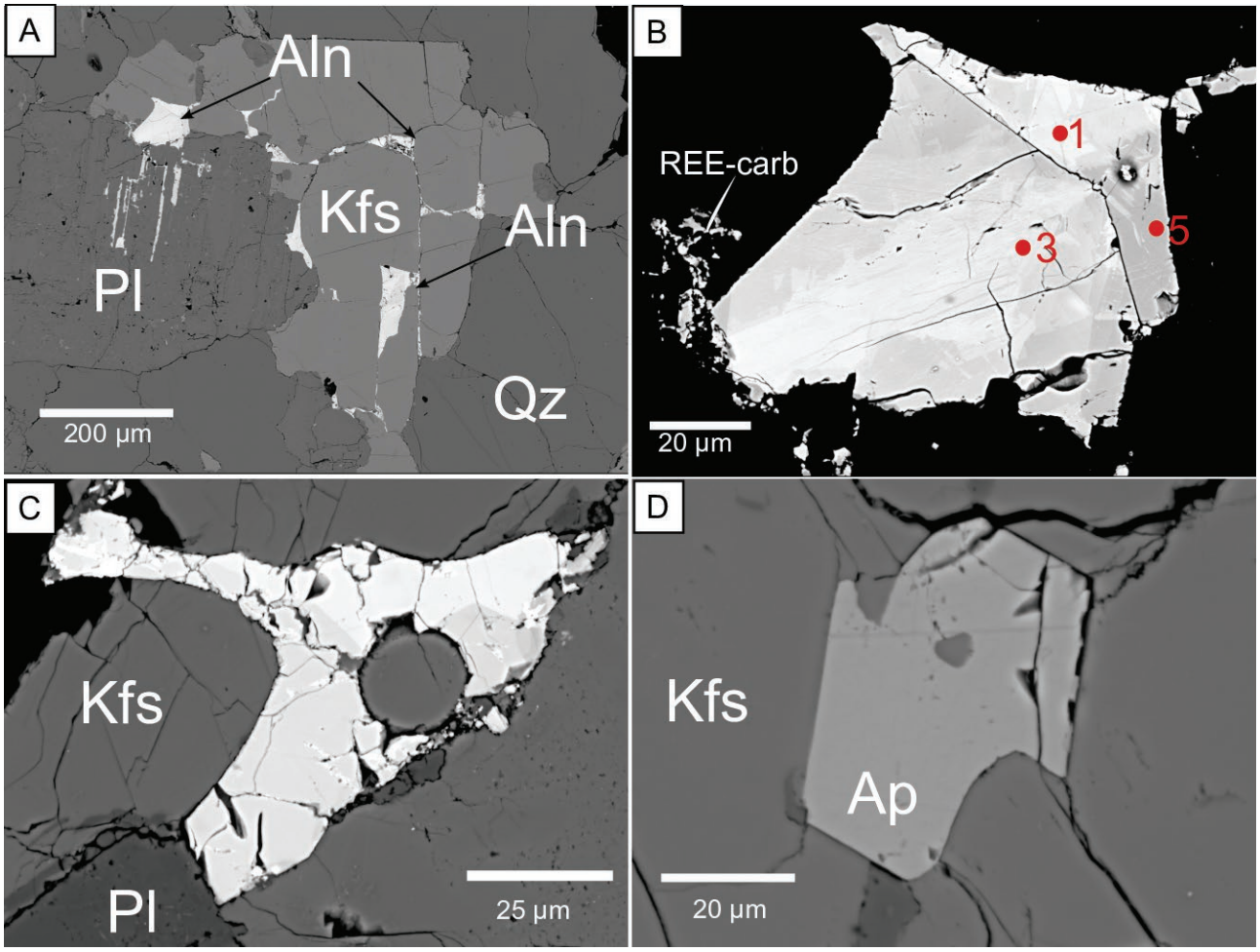

Fig. 8. Microtextures of allanite and apatite in ZHG. **A** — Network of allanite filling in fissures K-feldspar and plagioclase; **B** — Allanite showing pronounced patchy zonation with BSE-brighter inner zones and BSE-darker outer zones; **C** — Irregular, grainy allanite apparently replacing K-feldspar; note irregular BSE zonation; **D** — strongly anhedral apatite grain hosted by perthitic K-feldspar phenocryst.

the entirely reequilibrated zircon is often impossible (Fu et al. 2009), since in the latest stages of melt evolution magmatic and hydrothermal processes overlaps.

The relict, Hf-enriched, and NESC-free Zrn2 grains are likely entirely recrystallized phases (e.g., Fig. 4D, E) – in contrast, in the strongly heterogeneous grains of Zrn2, the NESCs have been redistributed by the interaction between mineral and fluid. The range of microtextures and partly overlapping composition of Zrn1 and Zrn2 represents various extents of fluid-aided magmatic–hydrothermal dissolution–reprecipitation, and removal of U, Y, HREE and other NESC. The elevated F and/or Cl and As (Supplementary material S3) support the fluid-rich environment for zircon growth or alteration (Breiter et al. 2009, 2014; Förster et al. 2011). The preserved high Y+REE's contents in the As-richest grains of Zrn2 may suggest local inhibition of Y and REE loss by isostructural chernovite substitution. The increased susceptibility of zircon to interaction with fluids is usually linked with long-lasting (tens of Myr) radiation damage (Geisler et al. 2007). However, that is not likely in the case of the ZHG zircon, where microtextures suggest a late-magmatic process, and most probably, it is related to the high content of NESC, which in general destabilizes crystalline lattice of zircon, and facilitates alteration (van Lichtervelde et al. 2009; Mahdy 2021).

Contrasting origin and evolution of xenotime and monazite

In the ZHG, the modal abundance of xenotime is higher than monazite, which is generally quite common in evolved peraluminous granites (Hetherington et al. 2008) but contrasts with the typical assemblage in S-type Variscan suites in the Western Carpathians (Broska et al. 2012) and emphasizes high (Y+HREE)/LREE ratio in the parental magma.

The distribution of xenotime along the zircon fragments suggests its growth coevally or subsequently to zircon fracturing. The genetic relationship between xenotime and zircon was described in many evolved granites and pegmatites (René 2014; Broska & Kubiš 2018; Mahdy 2021) and may result

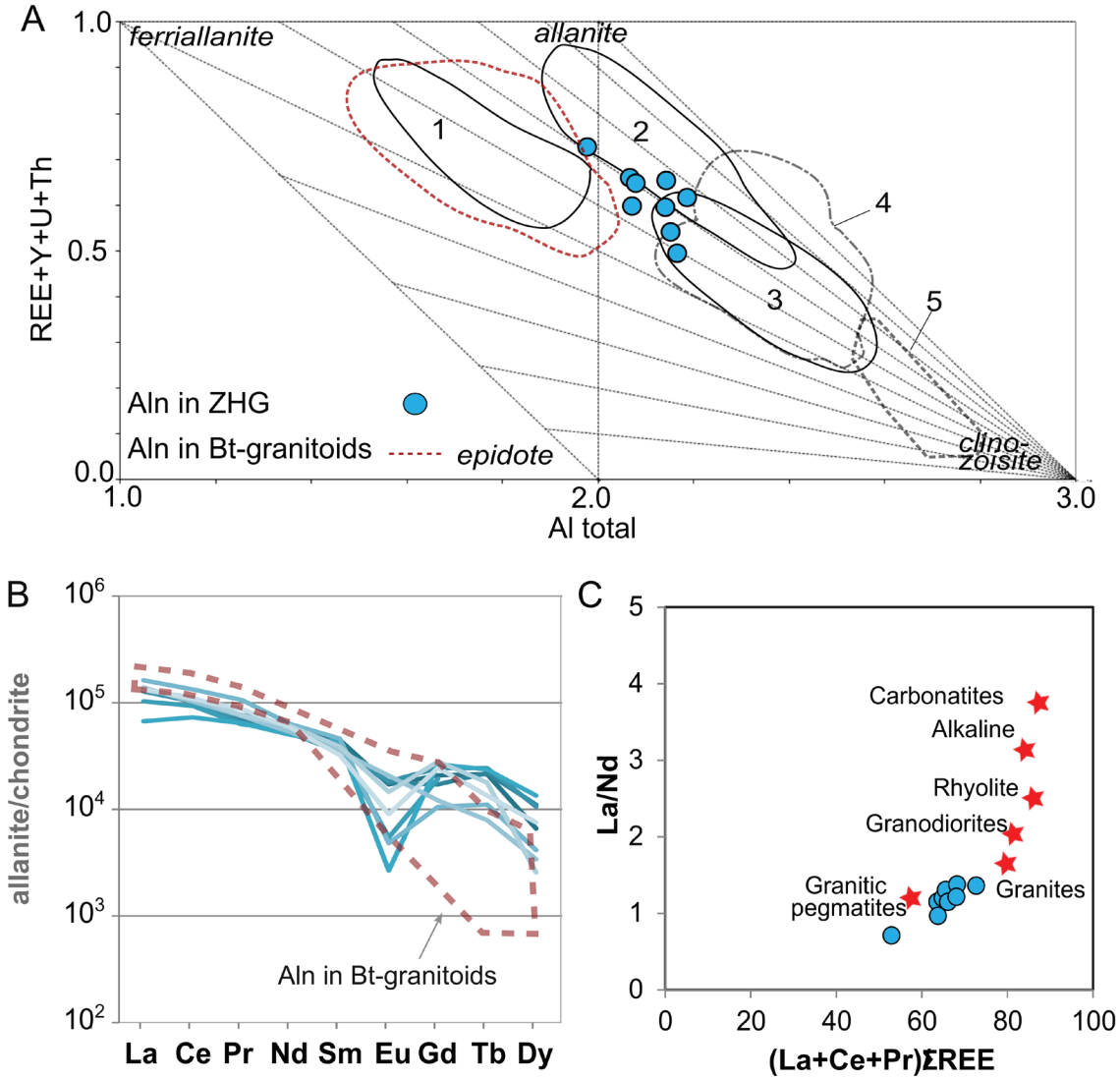

Fig. 9. Chemical composition of allanite in the ZHG. **A** — Al_{tot} vs REE+Y+U+Th (apfu) plot by Petrík et al. (1995) with fields of allanite of different origin: 1 – metaluminous granitoids emplaced at 3–4 kbar; 2 – peraluminous granitoids; 3 – metaluminous granitoids emplaced at 6–10 kbar; 4 – product of monazite alteration; 5-product of xenotime alteration (fields 1,2,3 after Broska et al. 2012, fields 4&5 after Budzyń et al. 2017). Dashed red line border the field of primary allanite in hosting Prašivá granodiorite (Maraszewska, unpublished data); **B** — Chondrite-normalized REE pattern of ZHG allanite- red field is typical composition of allanite in hosting Bt-granodiorites-tonalites; **C** — La/Nd vs La+Ce+Pr/(REE) (atomic%) showing LREE relations in allanite in different igneous rocks (modified after Fleischer 1985; Gieré & Sorensen 2004).

from their co-crystallization, but mainly from the breakdown of pre-existing zircon. The rare euhedral, concentric zoned xenotime with sharp contact with coexisting zircon (Fig. 4A) could have formed in a magmatic environment; anyway, the irregular or even pseudomorphic morphology of the most xenotime grains (Fig. 4B, D–F), as well as depletion in Y, U, P and HREE in coexisting relict Zrn2, advocates for secondary growth of xenotime at the expense of zircon (Franz et al. 2015; Mahdy 2021). However, the volume of zircon necessary to have been dissolved is unrealistically large, and at least part of the P, U and Y+HREE budget had to be supplied externally, similarly as proposed by Wang et al. (2001):

$$(Y, HREE, U)\text{-rich } Zrn + PO_4^{3-}(melt, fluid) \rightarrow$$
$$\rightarrow U, Th, Y, HREE)\text{-poor } Zrn + Xtm + Thr$$

The chemical composition of the xenotime supports continuous magmatic to hydrothermal crystallization; it varies from a composition typical for igneous xenotime in peraluminous suites (high U and low U/Th(wt%) <0.5 (Fig. 6A) and flat MREE–HREE pattern (Fig. 6D); low Gd/Yb (Fig. 6E) to a secondary or hydrothermal composition (low and scattered U and U/Th (Fig. 6A), variable enrichment in MREE with respect to HREE (Fig. 6D), high Gd/Yb and Y/Dy (Fig. 6E; Förster 1998b; Kositcin et al. 2003; McNaughton & Rasmussen 2018; Breiter & Förster 2021). The involvement of

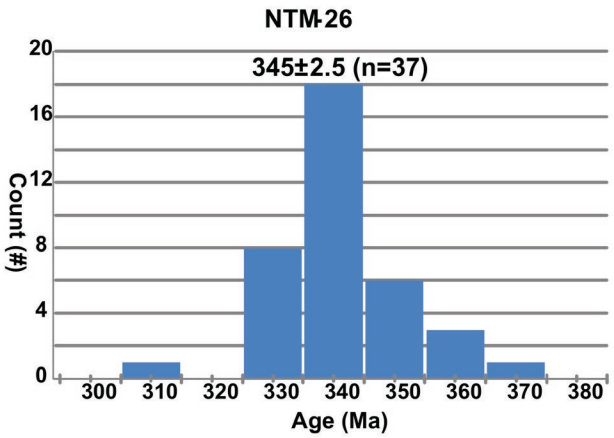

Fig. 10. Histogram showing monazite U–Th–total Pb dating results of the ZHG.

hydrothermal fluids in xenotime crystallization is also suggested by an elevated content of arsenic (Fig. 6F; Breiter et al. 2009). After all, the high variability of xenotime compositions likely reflects the local chemical environment related to heterogeneous fluid composition (Franz et al. 2015).

In contrast to the xenotime, the monazite in the ZHG is hosted by plagioclase phenocrysts and does not coexist with zircon; apart from the crystals resorption, the crystals mostly preserved tabular habit and sector zoning in cores characteristic for primary magmatic origin (Fig. 7A–C; Catlos 2013; Schulz 2021) and seems to precede zircon and xenotime in order of crystallization.

The igneous origin of the monazite is supported by its high Th content exceeding 5 wt% (Fig. 6A; late, hydrothermal or secondary monazite is usually <1.0 wt% ThO_2; Schandl & Gorton 2004), and moderate La/Ce, La/Nd, and La/Gd (Wark & Miller 1993). Predominant cheralite-type substitution (Fig. 6C) as well as relatively high U content (Fig. 6A, B) in apparently unaltered Mnz1 are typical for the monazite in differentiated peraluminous magmas (Förster 1998a; Pérez-Soba et al. 2014; Breiter & Förster 2021). The Mnz1 crystallization temperature estimates (Pyle et al. 2001) based on the X_{Y+HREE} content (0.071–0.095) are from 520 to 610 °C, what is in range of monazite in peraluminous suites (Breiter & Förster 2021), but these estimates should be treated with caution due to possible disequilibrium between monazite and xenotime connected with non-simultaneous crystallization, as well as the still not fully recognized effect of Th and Ca, Si and U on the Y+HREE partition into monazite (Seydoux-Guillaume et al. 2002; Mako et al. 2023). The altered rims and patches (Mnz2) show preferential retention of Th+Si and removal of U+Ca (Fig. 6B) and are typical for A-type granite huttonite enrichment (Breiter & Förster 2021). The variable depletion in X_{Y+HREE} content in Mnz2 (0.043–0.067 apfu), resulting in lower temperature estimates (370–510 °C;), together with the decrease in U, is in accordance with observations on the behaviour of the ZHG zircon during alteration, however, overall quite similar REE's patterns of Mnz1 and Mnz2 (Fig. 6D) imply, that the alteration did not significantly affect the mobility of particular REE's. Nevertheless, elevation in F up to >0.8 wt% in the ZHG monazite is extraordinary.

The unusually F-rich monazite was reported as a secondary effect of fluorapatite dissolution in hydrothermal Sn deposits (Catlos & Miller 2017); however, no spatial relation of monazite with apatite in the ZHG, and overall orthomagmatic characteristic of the Mnz1 rather excludes such a scenario. Nevertheless, high F and REE phosphates also occur in fluorine-rich pegmatite systems (Hetherington & Harlov 2008; Bastos Neto et al. 2012), which fits the "pegmatite-like" signature displayed by the zircon and xenotime and reflects the high activity of F during the monazite growth.

Allanite in ZHG: evidence of fluid-driven REE mobilization

The textural position of allanite as a net of veinlets within fissures in feldspars (Fig. 8A–C) reminds documented textures of late-magmatic or secondary allanite filling dissolution cavities (Anenburg et al. 2015) and is consistent with crystallization coevally, or subsequently, to deformation along with induced by late-magmatic fluids reaction of coexisting plagioclase and biotite with REE in melt/fluid (Skrzypek et al. 2020). The breakdown of plagioclase to albite+muscovite supplied Ca, whereas the replacement of biotite by muscovite+chlorite served as a source of Fe (Broska et al. 2005; Budzyń et al. 2017; Skrzypek et al. 2020). In the frame of TS granitoids, allanite resembles late-stage allanite formed in peraluminous suites (Fig. 9A); the whole-rock low Ca and high ASI (Supplementary Material S2) destabilizes orthomagmatic allanite in favour of monazite (Petrík & Broska 1994). The secondary corona structures of REE-fluorapatite–allanite–epidote around metasomatically altered monazite (Broska et al. 2005) are not observed in the ZHG, which indicates that REE released during monazite alteration were mobilized by fluids in thin section scale, alternatively or supplied by the fluids itself. The late-magmatic or hydrothermal crystallization of the allanite in a fluid-dominated regime is supported by extremely low Th concentrations, very low La/Nd <1.5 (atomic%) resembling one in allanite in pegmatites (Fig. 9C) and elevated Mn, Y and MREE (Supplementary material S5) indicating high water content (Hoshino et al. 2006) and/or Y and MREE enriched fluid (Anenburg et al. 2015). Consequently, the allanite in the ZHG is the latest crystallized mineral, indicating the circulation of Y+REE enriched, reactive fluids coevally with the sub-solidus deformation.

Deciphering melt and fluid composition

The microtexture of the ZHG shares some similarities with "two-phase" or "porphyritic" granite, recognized in several shallow-level, composite intrusions (Cobbing et al. 1986; Schaltegger et al. 2005; Štemprok et al. 2008;). These granites are characterized by bimodal to polymodal grain size texture,

defined by earlier crystallized, medium-grained mineral population, disrupted and penetrated by second-stage fine-crystalline and poikilitic matrix. These features are observed in ZHG, as very fine-grained matrix overflowing and penetrating brecciated phenocrysts (Fig. 2B) and local presence of late, coarse-grained muscovite and quartz (Fig. 2C, E). The embayed grain boundaries and droplet-like quartz inclusions of plagioclase and K-feldspars phenocrysts on contact with matrix assemblage, as well as late-stage quartz and muscovite, indicate relatively high magmatic temperatures of intrusions. The "two-phase" granite microtexture reflects devolatization and volatiles escape from magma crystallizing at the shallow crustal level: fine-grained microgranitic texture is linked with rapid nucleation due to H_2O loss and undercooling, whereas the large muscovite and quartz reflect latest stage growth in a fluid-rich environment (Štemprok et al. 2008); the brittle deformation of the phenocrysts indicate the dynamic and rapid character of this process. Chemically, the ZHG corresponds to highly fractionated peraluminous granite, defined by the high content of SiO_2, high ASI and depletion in CaO, FeO_t, MgO and TiO_2 (Supplementary Material S2) as well as low Nb/Ta (Ballouard et al. 2016); however, the depletion in P_2O_5 is in contradiction to the typical differentiation trend of peraluminous granite suites and reminds evolution of metaluminous magmas (Broska et al. 2004).

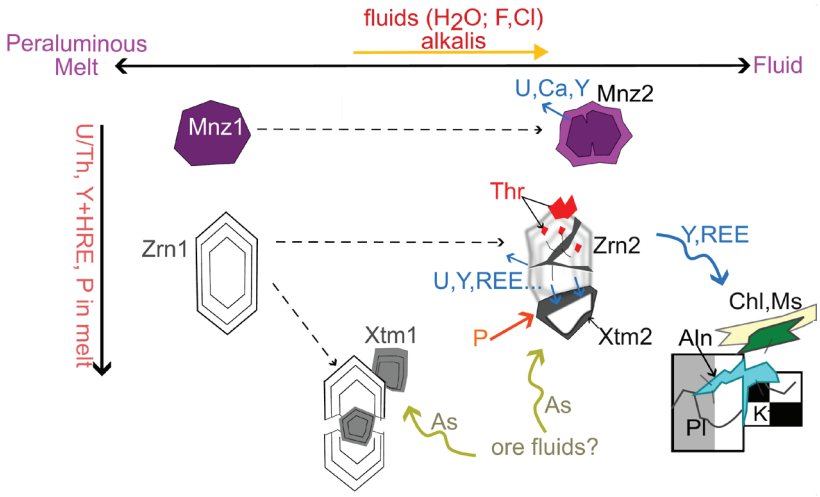

Fig. 11. Schematic model of evolution of the accessory mineral assemblage in the ZHG. Monazite has likely crystallized as the earliest phase from F-rich peraluminous magma. Progressive increase of Y+U+HREE in melt has caused neocrystallization or recrystallization of Zrn1, and following euhedral xenotime. The exsolution of volatile-oversaturated and alkali-enriched melt altered Mnz1 to Th and Si-rich, U, Ca, Y depleted Mnz2, and caused the dissolution of Zrn1-reprecipitation of Zrn2; released U, Y+HREE, and P from P-enriched feldspars stabilized secondary xenotime and possibly also thorite. Arsenic enrichment in zircon and xenotime implies circulation of As-bearing fluids, likely connected with high-temperature ore mineralization within LTP. Allanite formed in latest stages by transport of REE-bearing fluids and their reaction with rock forming minerals (mostly plagioclase and chloritized biotite).

The overall composition of the Mnz1–Zrn–Xtm assemblage in ZHG points to a progressive increase of U, Y and HREE in volatile-enriched melt (Fig. 11), characteristic of highly evolved peraluminous systems or pegmatites, produced by the extensive fractional crystallization (Pérez-Soba et al. 2014), or local liquid–liquid immiscibility (van Lichtervelde et al. 2021). The alteration textures shown, especially by Zrn2 and Mnz2, point to their origin from melt/fluid interaction, and depletion in U as well as Y+HREE in altered domains indicates the mobilization of these elements. The diversity of xenotime microtextures and chemistry reflects prolonged growth along the transition from melt-dominated to fluid-dominated regime, coeval with Zrn1 dissolution (Fig. 11). Finally, local crystallization of secondary allanite within the altered and brecciated feldspars is evidence for syn-deformational circulation of the reactive, REE transporting fluids.

In the earliest magmatic stages, a crucial factor controlling the accessory mineral assemblage was high ASI, water and fluorine content in the melt. The monazite crystallization before zircon was due to low and high solubility, respectively, in silica-, alumina-, and halogen-rich melts (Boehnke et al. 2013; Gervasoni et al. 2016). High ASI of melt supports partial partitioning of P into feldspars, which can be expelled, forming secondary fluorapatite inclusions (Broska et al. 2004). The stabilization of the fluorapatite exsolutions (Broska & Kubiš 2018) and the presence of fluorine in all accessory phases (Supplementary materials 3–6) point to exceptionally high F activity during magmatic and metasomatic evolution of the ZHG. Fluorine-rich melts/fluids are able to mobilize components such as HFSE and REE which are regarded as immobile during hydrothermal alteration (Williams-Jones et al. 2012; Migdisov & Williams-Jones 2014), and fractionate the HREE from LREE (Tsay et al. 2014; Li et al. 2022) as well as U and Th (Keppler & Wyllie 1990) which is documented in ZHG by predominance of HREE- and U-bearing phases. Moreover, zircon crystallized in the high F environment tends to incorporate high quantities of NESC (René 2014; Park et al. 2016). However, fluorine also supports xenotime growth at the expense of zircon (Hetherington et al. 2008). The additional factor for the metasomatic response of the accessory minerals in the ZHG and its subtle shift towards A-type magma typology (suggested by P deficiency in whole rock and in zircon, enrichment in HREE in the xenotime, and presence of thorite) are alkalis. The replacement of oligoclase phenocrysts by secondary albite and muscovite (Fig. 2F) and the formation of the muscovite+K-feldspar in the matrix (Fig. 2B–E) suggest the increased Na and K contents in the system at the magmatic–hydrothermal transition. Alkali- and halogen-bearing melts and fluids are able to mobilize P, U and Y+HREE from recrystallized zircon (Kubeš et al. 2021; Harlov et al.2023)

and stabilize the secondary Y-enriched thorite and xenotime (Förster 2006). Moreover, the alteration of monazite by alkaline fluids results in an increase in Th/U ratio and X_{Hutt}, and removal of U, Y and Ca (Harlov & Hetherington 2010). Last but not least, the phosphorus solubility in an alkaline environment is much lower than in a peraluminous environment (Piccoli & Candela 2002), which would explain the preferential precipitation of the xenotime.

Petrogenetic implications

The accessory mineral assemblage in the ZHG records a complex interplay of melt- and fluid-dominated processes in the final stages of magmatic evolution and shares several mineralogical features with one described in highly fractionated granitic and pegmatite systems. The highly evolved peraluminous magmas often have a high content of alkalies and evolve towards A-type signatures (Thomas et al. 2006; Pérez-Soba & Villaseca 2010) or undergo local scale immiscibility, forming strongly peraluminous and strongly alkaline fluid-rich magmas, which controls protracted variations of trace element concentrations (Thomas et al. 2006; van Lichtervelde et al. 2021). The presence of evolved magmatic systems in LTP is indicated by numerous muscovite and two-mica leucogranite bodies (Fig. 1C), as well as aplitic and pegmatite veins, locally containing uraninite (Majzlan et al. 2020a, b), Nb–Ta mineralization (e.g., Sopotnická Dolina; Uher et al. 1998a, b) and beryl (Pitoňák & Janák 1983). However, the other leucogranite bodies inboard the LTP, despite high peraluminosity, leucocratic character and lower REE and Zr contents than Prašiva or Ďumbier types, are far older (~350 Ma; Maraszewska et al. 2021) and do not show as effective LREE/HREE fractionation (Fig. 3B), P-depletion (Fig. 3A) and lack of the "two-phase" granite-like fabric but the body in the Klinisko ore deposits shows local greisenization (Maraszewska et al. 2019b; Maraszewska, unpublished data).

A local formation of the residual melts in composite, hybrid plutons is explained by advanced stages of magmatic differentiation and does not require the contribution of an exclusively crustal source (Pérez-Soba & Villaseca 2010). The Bt-granodiorite-granite of the Prašivá type likely derives from water-rich magmas from intermediate-felsic metaigneous and metasedimentary sources and contains abundant allanite or monazite, as well as early-magmatic apatite (Maraszewska et al. 2021, 2022). The extensive fractional crystallization of these accessory minerals, as well as plagioclase and biotite, could form peraluminous, U, HREE-rich, low-in-P residual melts, which is supported by the linear trend of P_2O_5 vs SiO_2 of the Prašivá type and ZHG (Fig. 3A). The age 345 Ma of magmatic monazite in the ZHG (Fig. 10, Supplementary Material S7) suits the scenario of the prolonged growth of the pluton by successive emplacement of multiple magma pulses, gradually changing composition from more mafic to felsic (Maraszewska et al. 2022), but contradicts its derivation from the 352–351 Ma Prašivá magma, since the over 6 Myr lasting crystallization at the emplacement level is unlikely. Nevertheless, Visean imprint is recorded in Prašivá type in rims of zircon (Maraszewska et al. 2022) and age 343±8.2 of subsolidus titanite (Uher et al. 2019), indicating the activity of high-temperature fluids in that time.

On the other hand, the highly peraluminous, fluid- and Y+HREE-enriched magmas are also produced during anatexis of solely upper crustal sources, as metapelites, or felsic metaigneous rocks (Nabelek & Glascock 1995, Villaros et al. 2009); indeed, the ZHG shares several features with garnet-leucogranites emplaced within metamorphic complex and originating from non-equilibrium water-absent melting of biotite- and muscovite-rich source (Petrík & Konečný 2009). However, in the ZHG monazite Tournaisian and older dates are rare and subordinately distributed, which distinguishes it from the garnet-leucogranites, in which inherited, metamorphic, ~355 Ma monazite predominates, and Visean (346±3 Ma) imprint was constrained only in magmatic/altered U- and Y-rich zones (Petrík & Konečný 2009). In the mobile, low-temperature (<650 °C according to Zr saturation temperatures and X_{Y+HREE} monazite geothermometry), peraluminous magmas such as the ZHG, the degree of the preservation of the inherited monazite should be high (Rubatto et al. 2006; Martins et al. 2009). Consequently, although our data cannot clearly define the origin of the ZHG, it most likely represents an independent pulse of late-stage magma from the long-living magma chamber.

Metallogenic implications

The elevated content of As_2O_5 in zircon and xenotime (Supplementary materials S3 and S4; Fig. 6F) is remarkable and could be related to As-rich, oxidized, ore-related fluids (Ondrejka et al. 2007; Breiter et al. 2009; Förster et al. 2011), which can be likely linked to the adjacent Magurka ore deposits. Although metamorphic versus magmatic origin of the Variscan ore mineralization is still unresolved (Chovan et al. 1996; Majzlan et al. 2020a), the monazite age of the ZHG is close to the timing of formation (351–343 Ma) of the uraninite-bearing pegmatites and the highest-temperature molybdenite mineralization stage in the LTP (Majzlan et al. 2020b). Moreover, the Prašivá granite in that area contains the S- and Sr-rich monazite (up to 1.5 and 2 wt%, respectively: Maraszewska, unpublished data). The content of fluorine in Prašivá type biotite ranges from b.d.l. in more mafic, up to 0.45 wt% in most differentiated lithofacies (Maraszewska, unpublished data), indicating progressive F enrichment in the melt, but also the high volatile budget in the parental granodioritic magma. The composite fabric of the ZHG, omnipresent evidence of the influence of reactive fluids, and overall composition of the accessory minerals, but especially the elevated content of halogens (Bastos Neto et al. 2012; Catlos & Miller 2017), the high NESC content in zircon and enrichment in As are fingerprints of the fertile felsic suites, associated with a wide range of metal associations such as Li–F (Förster et al. 2011); Nb–Ta (van Lichterwelde et al. 2009), W–Sn (Schaltegger et al. 2005) and

Au–Cu porphyries (Fu et al. 2009), which gives the strong arguments for the metallogenic potential of igneous differentiation in the LTP.

Conclusions

The detailed petrographic and mineralogical description of the peraluminous Zámostská Hoľa leucogranite presents the evolution of granitic melts along with magmatic–hydrothermal transition and highlights the complexity of the prolonged, composite petrogenesis of the granitoid pluton in the Low Tatra Mts. Finally, these findings provide new insights into the possible link of the granitic magmatism and associated fluid circulation and the development of giant ore deposit systems in the Low Tatra Mts.

Acknowledgements: This study was funded by grants from the Slovak Research and Development Agency VEGA 2/0075/20 and ERANET-MIN PEGMAT JTC-2021_174. We are grateful to Igor Petrík (ÚVZ SAV, Bratislava) and Jarosław Majka (AGH-UST, Uppsala) for helpful comments and recommendations, which were used for the final manuscript.

References

Amli R. & Griffin W. 1975: Microprobe analysis of REE minerals using empirical correction factors. *American Mineralogist* 60, 599–606.

Anenburg M., Katzir Y., Rhede D., Jöns N. & Bach W. 2015: Rare earth element evolution and migration in plagiogranites: a record preserved in epidote and allanite of the Troodos ophiolite. *Contributions to Mineralogy and Petrology* 169, 25. https://doi.org/10.1007/s00410-015-1114-y

Ballouard C., Poujol M., Boulvais P., Branquet Y., Tartèse R. & Vigneresse J.-L. 2016: Nb–Ta fractionation in peraluminous granites: A marker of the magmatic-hydrothermal transition. *Geology* 44, 231–234. https://doi.org/10.1130/g37475.1

Bastos Neto A.C., Pereira V.P., Pires A.C., Barbanson L. & Chauvet A. 2012: Fluorine-rich xenotime from the world-class Madeira Nb–Ta–Sn deposit associated with the albite-enriched granite at Pitinga, Amazonia, Brazil. Canadian Mineralogist 50, 1453–1466. https://doi.org/10.3749/canmin.50.6.1453

Bezák V., Jacko S., Janák M., Ledru P., Petrík I. & Vozárová A. 1997: Main Hercynian lithotectonic units of the Western Carpathians. In: Grecula P., Hovorka D. & Putiš M. (eds): Geological evolution of the Western Carpathians, 261–268.

Biely A. (Ed.), Beňuška P., Bezák V., Bujnovský A., Halouzka R., Ivanička J., Kohút M., Klinec A., Lukáčik E., Maglay J., Miko O., Pulec M., Putiš M. & Vozár J. 1992: Geological map of the Nízke Tatry Mts. 1:50,000. *Dionýz Štúr Institute of Geology*, Bratislava

Boehnke P., Watson E.B., Trail D., Harrison T.M. & Schmitt A.K. 2013: Zircon saturation re-revisited. *Chemical Geology* 351, 324–334. https://doi.org/10.1016/j.chemgeo.2013.05.028

Bonin B., Janoušek V. & Moyen J.F. 2020: Chemical variation, modal composition and classification of granitoids. *Geological Society of London Special Publications* 491, 9–51. https://doi.org/10.1144/SP491-2019-138

Breiter K. & Förster H.J. 2021: Compositional variability of monazite–cheralite–huttonite solid solutions, xenotime, and uraninite in geochemically distinct granites with special emphasis to the strongly fractionated peraluminous Li–F–P–Rich Podlesi Granite System (Erzgebirge/Krušné Hory Mts., Central Europe). *Minerals* 11, 127. https://doi.org/10.3390/min11020127

Breiter K., Čopjaková R. & Škoda R. 2009: The involvement of F, CO_2, and As in the alteration of Zr–Th–REE-bearing accessory minerals in the Hora Svaté Kateřiny A-Type Granite, Czech Republic. *Canadian Mineralogist* 47, 1375–1398. https://doi.org/10.3749/canmin.47.6.1375

Breiter K., Lamarao C.N., Borges R. & Dall´Agnol R. 2014: Chemical characteristic of zircon from A-type granites and comparison to zircon of S-type granites. *Lithos* 192–195, 208-225. https://doi.org/10.1016/j.lithos.2014.02.004

Broska I. & Kubiš M. 2018: Accessory minerals and evolution of tin-bearing S-type granites in the western segment of the Gemeric Unit (Western Carpathians). *Geologica Carpathica* 69, 483–497. https://doi.org/10.1515/geoca-2018-0028

Broska I. & Uher P. 2001: Whole-rock chemistry and genetic typology of the West-Carpathian Variscan granites. *Geologica Carpathica* 52, 79–90.

Broska I.,Williams C.T., Uher P., Konečný P. & Leichmann J. 2004: The geochemistry of phosphorus indifferent granite suites of the Western Carpathians, Slovakia: the role of apatite and P-bearing feldspar. *Chemical Geology* 205, 1–15. https://doi.org/10.1016/j.chemgeo.2003.09.004

Broska I., Williams C.T., Janák M. & Nagy G. 2005: Alteration and breakdown of xenotime-(Y) and monazite-(Ce) in granitic rocks of the Western Carpathians, Slovakia. *Lithos* 82, 71–83. https://doi.org/10.1016/j.lithos.2004.12.007

Broska I., Petrík I. & Uher P. 2012: Accessory minerals of granitoid rocks of the Western Carpathians. *Veda*, Bratislava.

Broska I., Petrík I., Be'eri–Shlevin Y., Majka J. & Bezák V. 2013: Devonian/Mississippian I-type granitoids in the Western Carpathians: A subduction-related hybrid magmatism. *Lithos* 162–163, 27–36. https://doi.org/10.1016/j.lithos.2012:12.014

Broska I., Janák M., Svojtka M., Yi K., Konečný P., Kubiš M., Kurylo S., Hrdlička M. & Maraszewska M. 2022: Variscan granitic magmatism in the Western Carpathians with linkage to slab break-off. *Lithos* 412–413, 106589. https://doi.org/10.1016/j.lithos.2021.106589

Budzyń B., Harlov D.E., Kozub-Budzyń G.A., & Majka J. 2017: Experimental constraints on the relative stabilities of the two systems monazite-(Ce)–allanite-(Ce)–fluorapatite and xenotime-(Y)–(Y,HREE)-rich epidote–(Y,HREE)-rich fluorapatite, in high Ca and Na–Ca environments under P–T conditions of 200–1000 MPa and 450–750 °C. *Mineralogy and Petrology* 111, 183–217. https://doi.org/10.1007/s00710-016-0464-0

Burda J., Klötzli U., Woskowicz-Ślęzak B., Li Q-L. & Liu Y. 2020: Inherited or not inherited: Complexities in dating the atypical 'cold' Chopok granite (Nízke Tatry Mountains, Slovakia). *Gondwana Research* 87, 138–161. https://doi.org/10.1016/j.gr.2020.05.018

Catlos E.J. 2013: Versatile Monazite: resolving geological records and solving challenges in materials science: Generalizations about monazite: Implications for geochronologic studies. *American Mineralogist* 98, 819–832. https://doi.org/10.2138/am.2013.4336

Catlos E.J. & Miller N. 2017: Speculations linking monazite compositions to origin: Llallagua tin ore deposit (Bolivia). *Resources* 6, 36. https://doi.org/10.3390/resources6030036

Catlos E., Broska I., Kohút M., Etzel T.M., Kyle J.R., Stockli D.F., Miggins D.P., Campos D. 2022: Geochronology, geochemistry, and geodynamic evolution of Tatric granites from crystalline exhumation (Tatra Mountains, Western Carpathians). *Geologica Carpathica* 73, 517–544. https://doi.org/10.31577/GeolCarp.73.6.1

Chovan M., Póč I., Jancsy P., Majzlan J., Krištín J. 1995: Sb–Au (As–Pb) mineralization of the Magurka deposit, Low Tatras. *Mineralia Slovaca* 27, 397–406 (in Slovak).

Chovan M., Slavkay M. & Michálek J. 1996: Ore mineralization of the Ďumbierske Tatry Mts. (Western Carpathians, Slovakia). *Geologica Carpathica* 47, 371–382.

Cobbing EJ., Mallick D., Pitfield P. & Teoh L. 1986: The granites of the South-East Asian tin belt. *Journal of the Geological Society London* 143, 537–550

Corfu F., Hanchar J.M., Hoskin P.W. & Kinny P.D. 2003: Atlas of zircon textures. *Reviews in Mineralogy and Geochemistry* 53, 469–500. https://doi.org/10.2113/0530469

Dávidová S. 1978: Mineralogy and petrography of Tatric crystallite pegmatites. *Mineralia Slovaca* 10, 127–146.

Dolejš D. & Zajacz Z. 2018: Halogens in silicic magmas and their hydrothermal systems. In: Harlov D. & Aranovich L. (eds.): The role of halogens in terrestrial and extraterrestrial geochemical processes. *Springer Geochemistry*, 431–543. https://doi.org/10.1007/978-3-319-61667-4_7

Erdmann S., Wodicka N., Jackson S.E. & Corrigan D. 2012: Zircon textures and composition: refractory recorders of magmatic volatile evolution? *Contributions to Mineralogy and Petrology* 165, 45–71. https://doi.org/10.1007/s00410-012-0791-z

Fleischer M. 1985: A summary of the variations in relative abundance of the lanthanides and yttrium in allanites and epidotes. *Bulletin of Geological Society of Finland* 57, 151–155.

Förster H.J. 1998a: The chemical composition of REE–Y–Th–U-rich accessory minerals in peraluminous granites of the Erzgebirge–Fichtelgebirge region, Germany. Part I: The monazite-(Ce) – brabantite solid solution series. *American Mineralogist* 83, 259–272.

Förster H.J. 1998b: The chemical composition of REE–Y–Th–U-rich accessory minerals in peraluminous granites of the Erzgebirge–Fichtelgebirge region, Germany. Part II: Xenotime. *American Mineralogist* 83, 1302–1315.

Förster H.J. 2006: Composition and origin of intermediate solid solutions in the system thorite–xenotimezircon–coffinite. *Lithos* 88, 35–55. https://doi.org/10.1016/j.lithos.2005.08.003

Förster H.J., Ondrejka M. & Uher P. 2011: Mineralogical responses to subsolidus alteration of granitic rocks by oxidizing As-bearing fluids: REE arsenates and As-rich silicates from the Zinnwald granite, eastern Erzgebirge, Germany. *Canadian Mineralogist* 49, 913–930. https://doi.org/10.3749/canmin.49.4.913

Franz G., Morteani G. & Rhede D. 2015: Xenotime-(Y) formation from zircon dissolution–precipitation and HREE fractionation: an example from a metamorphosed phosphatic sandstone, Espinhaço fold belt (Brazil). *Contributions to Mineralogy and Petrology* 170, 37. https://doi.org/10.1007/s00410-015-1191-y

Fu B., Mernagh T., Kita N., Kemp A. & Valley J. 2009: Distinguishing magmatic zircon from hydrothermal zircon: A case study from the Gidginbung high-sulphidation Au–Ag–(Cu) deposit, SE Australia. *Chemical Geology* 259, 131–142. https://doi.org/10.1016/j.chemgeo.2008.10.035

Gagnevin D., Daly J. & Kronz A. 2010: Zircon texture and chemical composition as a guide to magmatic processes and mixing in a granitic environment and coeval volcanic system. *Contributions to Mineralogy and Petrology* 159, 579–596. https://doi.org/10.1007/s00410-009-0443-0

Geisler T., Schaltegger U. & Tomaschek F. 2007: Re-equilibration of zircon in aqueous fluids and melts. *Elements* 3, 43–50. https://doi.org/10.2113/gselements.3.1.43

Gervasoni F., Klemme S., Rocha-Júnior E & Berndt J. 2016: Zircon saturation in silicate melts: a new and improved model for aluminous and alkaline melts. *Contributions to Mineralogy and Petrology* 171, 429–437. https://doi.org/10.1007/s00410-016-1227-y

Gieré R. & Sorensen S.S. 2004:Allanite and other REE-rich epidote-group minerals. *Reviews in Mineralogy and Geochemistry* 56, 431–493. https://doi.org/10.2138/gsrmg.56.1.431

Halter W.E. & Webster J.D. 2004: The magmatic to hydrothermal transition and its bearing on ore-forming systems. *Chemical Geology* 210, 1–6. https://doi.org/10.1016/j.chemgeo.2004.06.001

Harlov D.E. & Hetherington C.J. 2010: Partial high-grade alteration of monazite using alkali-bearing fluids: Experiment and nature. *American Mineralogist* 95, 1105–1108. https://doi.org/10.2138/am.2010.3525

Harlov D.E., Anczkiewicz R. & Dunkley D. J. 2023: Metasomatic alteration of zircon at lower crustal P–T conditions utilizing alkali- and F-bearing fluids: Trace element incorporation, depletion, and resetting the zircon geochronometer. *Geochimica et Cosmochimica Acta* 352, 222–235. https://doi.org/10.1016/j.gca.2023.05.011

Hetherington C.J. & Harlov D.E. 2008: Metasomatic thorite and uraninite inclusions in xenotime and monazite from granitic pegmatites, Hidra anorthosite massif, southwestern Norway: Mechanics and fluid chemistry. *American Mineralogist* 93, 806–820. https://doi.org/10.2138/am.2008.2635

Hetherington C.J., Jercinovic M.J., Williams M.L. & Mahan K. 2008: Understanding geologic processes with xenotime: Composition, chronology, and a protocol for electron probe microanalysis. *Chemical Geology* 254, 133–147. https://doi.org/10.1016/j.chemgeo.2008.05.020

Hók J., Pelech O., Teťák F., Németh Z. & Nagy A. 2019: Outline of the geology of Slovakia (W. Carpathians). *Mineralia Slovaca* 51, 31–60.

Hoshino M., Kimata M., Shimizu M., Nishida N., & Fujiwara T. 2006: Allanite-(Ce) in granitic rocks from Japan Genetic implications of patterns of REE and Mn enrichment. *Canadian Mineralogist* 44, 45–62. https://doi.org/10.2113/gscanmin.44.1.45

Hoskin P.W. & Ireland T.R. 2000: Rare earth element chemistry of zircon and its use as a provenance indicator. *Geology* 28, 627–630. https://doi.org/10.1130/0091-7613(2000)28%3C627:REECOZ%3E2.0.CO;2

Hoskin P.W., Kinny P., Wyborn D. & Chappell B. 2000: Identifying accessory mineral saturation during differentiation in granitoid magmas: an interpreted approach. *Journal of Petrology* 41, 1365–1396. https://doi.org/10.1093/petrology/41.9.1365

Kelly C.J., Harlov D.E., Schneider D.A., Jackson S.A. & Dubosq R. 2020: Experimental fluid-mediated alteration of zircon under lower greenschist facies conditions. *Canadian Mineralogist* 58, 247–265. https://doi.org/10.3749/canmin.1900041

Keppler H. & Wyllie P. 1990: Role of fluids in transport and fractionation of uranium and thorium in magmatic processes. *Nature* 348, 531–533. https://doi.org/10.1038/348531a0

Kohút M. & Larionov A.N. 2021: From subduction to collision: Genesis of the Variscan granitic rocks from the Tatric Superunit (Western Carpathians, Slovakia). *Geologica Carpathica* 72, 96–113. https://doi.org/10.31577/GeolCarp.72.2.2

Kohút M. & Nabelek P. 2008. Geochemical and isotopic (Sr, Nd and O) constraints on sources for Variscan granites in the Western Carpathians – implications for crustal structure and tectonics. *Journal of Geosciences* 53, 307–322.

Konečný P., Kusiak M.A. & Dunkley D.J. 2018: Improving U–Th–Pb electron microprobe dating using monazite age references. *Chemical Geology* 484, 22–35. https://doi.org/10.1016/j.chemgeo.2018.02.014

Kositcin N., McNaughton N.J., Griffin B., Fletcher I., Groves D. & Rasmussen B. 2003: Textural and geochemical discrimination between xenotime of different origin in the Archaean Witwatersrand Basin, South Africa. *Geochimica et Cosmochimica Acta* 67, 709–731. https://doi.org/10.1016/S0016-7037(02)01169-9

Kubeš M., Leichmann J., Wertich V., Mozola J., Holá M., Kanický V. & Škoda R. 2021: Metamictization and fluid-driven alteration triggering massive HFSE and REE mobilization from zircon and titanite: Direct evidence from EMPA imaging and LA-ICP-MS analyses. *Chemical Geology* 586, 120593. https://doi.org/10.1016/j.chemgeo.2021.120593

Li Z.-X., Zhang S.-B., Zheng Y.-F., Wu S.-T., Li W.-C., Sun F.-Y. & Liang T. 2022: Mobilization and fractionation of HFSE and REE by high fluorine fluid of magmatic origin during the alteration of amphibolite. *Lithos* 420–421, 106701. https://doi.org/10.1016/j.lithos.2022.106701

Magna T., Janoušek V., Kohút M., Oberli F. & Wiechert U. 2010: Fingerprinting sources of orogenic plutonic rocks from Variscan belt with lithium isotopes and possible link to subduction–related origin of some A–type granites. *Chemical Geology* 274, 94–107. https://doi.org/10.1016/j.chemgeo.2010.03.020

Mahdy N.M. 2021: Textural and chemical characteristics of zircon, monazite, and thorite, Wadi Al-Baroud area, Eastern Desert of Egypt: Implication for rare metal pegmatite genesis. *Ore Geology reviews* 136, 104225. https://doi.org/10.1016/j.oregeorev.2021.104225

Majzlan J., Chovan M., Hurai V. & Luptáková J. 2020a: Hydrothermal mineralisation of the Tatric Superunit (Western Carpathians, Slovakia): I. A review of mineralogical, thermometry and isotope data. *Geologica Carpathica* 71, 85–112. https://doi.org/10.31577/GeolCarp.71.2.1

Majzlan J., Chovan M., Kiefer S., Gerdes A., Kohút M., Siman P., Konečný P., Števko M., Finger F., Waitzinger M., Biroň A., Luptáková J., Ackerman L. & Hora J. 2020b: Hydrothermal mineralisation of the Tatric Superunit (Western Carpathians, Slovakia): II. Geochronology and timing of mineralisations in the Nízke Tatry Mts. *Geologica Carpathica* 71, 113–133. https://doi.org/10.31577/GeolCarp.71.2.2

Mako C.A., Caddick M.J., Law R.D. & Thigpen J. 2023: Monazite–xenotime thermometry: a review of best practices and an example from the Caledonides of northern Scotland. *Geological Society of London Special Publications* 537, 246. https://doi.org/10.1144/sp537-2022-246

Maraszewska M., Broska I. & Kurylo S. 2019a: Hybrid I/S nature of Prašivá granite type, Low Tatra pluton: Evidence from mineralogical data. In: Proceedings of Geologica Carpathica 70 Conference. Bratislava, 91–94.

Maraszewska M., Kurylo S., Broska I. & Bezák V. 2019b: Rock-forming and accessory minerals from contrasting granite types of the Ďumbier crystalline complex (Nízke Tatry Mts., Western Carpathians. In: Mineralogical–Petrological Conference Petros 2019: Book of abstracts, 40.

Maraszewska M., Broska I., Kohút M., Yi K., Konečný P. & Kurylo S. 2021: Multistage evolution of granitoid magmatism in the Low Tatra Mts. – Western Carpathians based on preliminary SHRIMP zircon and U–Th–Pb monazite geochronology records. In: CETEG 2021: Book of Abstracts, 84.

Maraszewska M., Broska I., Kohút M., Yi K-W., Konečný P. & Kurylo S. 2022: The Ďumbier–Prašivá High K calc-alkaline granite suite (Low Tatra Mts., Western Carpathians): insights into their evolution from geochemistry and geochronology. *Geologica Carpathica* 73, 273–291. https://doi.org/10.31577/GeolCarp.73.4.1

Martins L., Vlach S.R. & De Assis Janasi V 2009: Reaction microtextures of monazite: Correlation between chemical and age domains in the Nazaré Paulista migmatite, SE Brazil. *Chemical Geology* 261, 271–285. https://doi.org/10.1016/j.chemgeo.2008.09.020

McDonough W.F. & Sun S.S. 1995: The composition of the Earth. *Chemical Geology* 120, 223–253.

McNaughton N.J. & Rasmussen B. 2018: Geochemical characterization of xenotime formation enviroments using U–Th. *Chemical Geology* 484, 109–119. https://doi.org/10.1016/j.chemgeo.2017.08.016

Migdisov A.A. & Williams-Jones A.E. 2014: Hydrothermal transport and deposition of the rare earth elements by fluorine-bearing aqueous liquids. *Mineralium Deposita* 49, 987–997. https://doi.org/10.1007/s00126-014-0554-z

Montel J.-M. 1993: A model for monazite/melt equilibrium and application to the generation of granitic magmas. *Chemical Geology* 110, 127–146. https://doi.org/10.1016/0009-2541(93)90250-M

Nabelek PI. & Glascock M. 1995: REE-depleted leucogranites, Black Hills, South Dakota: a consequence of disequilibrium melting of monazite-bearing schists. *Journal of Petrology* 36, 1055–1071. https://doi.org/10.1093/petrology/36.4.1055

Ondrejka M., Uher P., Pršek J. & Ozdín D. 2007: Arsenian monazite-(Ce) and xenotime-(Y), REE arsenates and carbonates from the Tisovec–Rejkovo rhyolite, Western Carpathians, Slovakia: Composition and substitutions in the (REE,Y)XO4 system (X= P, As, Si, Nb, S). *Lithos* 95, 116–129. https://doi.org/10.1016/j.lithos.2006.07.019

Park C., Song Y., Chung D., Kang I.M., Khulganakhuu C. & Yi K. 2016: Recrystallization and hydrothermal growth of high U–Th zircon in the Weondong deposit, Korea: record of post-magmatic alteration. *Lithos* 260, 268–285. https://doi.org/10.1016/j.lithos.2016.05.026

Pérez-Soba C. & Villaseca C. 2010: Petrogenesis of highly fractionated I-type peraluminous granites: La Pedriza pluton (Spanish Central System). *Geologica Acta* 8, 131–149. https://doi.org/10.1344/105.000001527

Pérez-Soba C., Villaseca C., Del Tanago J. & Nasdala L. 2007: The composition of zircon in the peraluminous hercynian granites of the Spanish Central System Batholith. *Canadian Mineralogist* 45, 509–527. https://doi.org/10.2113/gscanmin.45.3.509

Pérez-Soba C., Villaseca C., Orejana D. & Jeffries T. 2014: Uranium-rich accessory minerals in the peraluminous and perphosphorous Belvís de Monroy pluton (Iberian Variscan belt). *Contributions to Mineralogy and Petrology* 165, 1008. https://doi.org/10.1007/s00410-014-1008-4

Petrík I. & Broska I. 1994: Petrology of two granite types from the Tribeč Mountains, Western Carpathians: an example of allanite (+magnetite) versus monazite dichotomy. *Geological Journal* 29, 59–78. https://doi.org/10.1002/gj.3350290106

Petrík I. & Kohút M. 1997: The evolution of granitoid magmatism during the Hercynian Orogen in the Western Carpathians. In: Grecula P., Hovorka D. & Putiš M. (eds.): Geological evolution of the Western Carpathians. Bratislava, 235–252.

Petrík I. & Konečný P. 2009: Metasomatic replacement of inherited metamorphic monazite in a biotite-garnet granite from the Nízke Tatry Mountains, Western Carpathians, Slovakia: Chemical dating and evidence for disequilibrium melting. *American Mineralogist* 94, 957–974. https://doi.org/10.2138/am.2009.2992

Petrík I., Broska I., Lipka J. & Siman P. 1995: Granitoid allanite-(Ce): substitution relations, redox conditions and REE distributions (on an example of I-type granitoids, Western Carpathians, Slovakia). *Geologica Carpathica* 46, 79–94.

Piccoli P. & Candela P. 2002: Apatite in Igneous Systems. *Reviews in Mineralogy and Geochemistry* 48, 255–292. https://doi.org/10.2138/rmg.2002.48.6

Pitoňák P. & Janák M. 1983: Beryl – a new mineral of the Low Tatras pegmatites. *Mineralia Slovaca* 15, 231–233 (in Slovak).

Plašienka D., Grecula P., Putiš M., Kováč M. & Hovorka D. 1997: Evolution and structure of the Western Carpathians: An overview. In: Grecula P., Hovorka D. & Putiš M. (eds): Geological evolution of the Western Carpathians. Bratislava, 1–24.

Pointer C.M., Ashworth J.R. & Ixer R. 1988: The zircon-thorite mineral group in metasomatized granite, Ririwai, Nigeria 2. zoning, alteration and exsolution in zircon. *Mineralogy and Petrology* 39, 21–37.

Poller U., Huth J., Hoppe P. & Williams I.S. 2001: Ree, U, Th, and Hf distribution in zircon from Western Carpathian Variscan Granitoids: a combined cathodoluminescence and ion microprobe study. *American Journal of Science* 301, 858–876. https://doi.org/10.2475/ajs.301.10.858

Pyle J.M., Spear F.S., Rudnick R.L. & McDonough W.F. 2001: Monazite–xenotime–garnet equilibrium in metapelites and a new monazite–garnet thermometer. *Journal of Petrology* 42, 2083–2107. https://doi.org/10.1093/petrology/42.11.2083

René M. 2014: Composition of coexisting zircon and xenotime in rare-metal granites from the Krušné Hory/Erzgebirge Mts. (Saxothuringian Zone, Bohemian Massif). *Mineralogy and Petrology* 108, 551–569. https://doi.org/10.1007/s00710-013-0318-y

Rubatto D., Hermann J. & Buick I. 2006: Temperature and bulk composition control on the growth of monazite and zircon during low-pressure anatexis (Mount Stafford, Central Australia). *Journal of Petrology* 47, 1973–1996. https://doi.org/10.1093/petrology/egl033

Sasvári T. & Rozložník L. 1993: Structural-metallogenetic assumptions of scheelite mineralization of the southeastern part of the Low Tatras. *Mineralia Slovaca* 25, 320–322 (in Slovak).

Schaltegger U., Pettke T., Audétat A., Reusser E. & Heinrich C. 2005: Magmatic-to-hydrothermal crystallization in the W–Sn mineralized Mole Granite (NSW, Australia). *Chemical Geology* 220, 215–235. https://doi.org/10.1016/j.chemgeo.2005.02.018

Schandl E.S. & Gorton M. 2004: A textural and geochemical guide to the identification of hydrothermal monazite: criteria for selection of samples for dating epigenetic hydrothermal ore deposits. *Economic Geology* 99, 1027–1035. https://doi.org/10.2113/gsecongeo.99.5.1027

Schulz B. 2021: Monazite Microstructures and Their Interpretation in Petrochronology. *Frontiers in Earth Science* 9, 668566. https://doi.org/10.3389/feart.2021.668566

Seydoux-Guillaume A., Wirth R., Heinrich W. & Montel J.-M. 2002: Experimental determination of thorium partitioning between monazite and xenotime using analytical electron microscopy and X-ray diffraction Rietveld analysis. *European Journal of Mineralogy* 14, 869–878. https://doi.org/10.1127/0935-1221/2002/0014-0869

Simons B., Andersen J., Shail R. & Jenner F. 2017:Fractionation of Li, Be, Ga, Nb, Ta, In, Sn, Sb, W and Bi in the peraluminous Early Permian Variscan granites of the Cornubian Batholith: precursor processes to magmatic–hydrothermal mineralisation. *Lithos* 278, 491–512. https://doi.org/10.1016/j.lithos.2017.02.007

Skrzypek E., Sakata S. & Sorger D. 2020: Alteration of magmatic monazite in granitoids from the Ryoke belt (SW Japan): Processes and consequences. *American Mineralogist* 105, 538–554. https://doi.org/10.2138/am-2020-7025

Štemprok M., Dolejš D., Muller A. & Seltmann R. 2008: Textural evidence of magma decompression, devolatilization and disequilibrium quenching: an example from the Western Krušné hory/Erzgebirge granite pluton. *Contributions to Mineralogy and Petrology* 155, 93–109. https://doi.org/10.1007/s00410-007-0229-1

Thomas R., Webster J., Rhede D., Seifert W., Rickers K., Förster H., Heinrich W. & Davidson P. 2006: The transition from peraluminous to peralkaline granitic melts: Evidence from melt inclusions and accessory minerals. *Lithos* 91, 137–149. https://doi.org/10.1016/j.lithos.2006.03.013

Tsay A., Zajacz Z. & Sanchez-Valle C. 2014: Efficient mobilization and fractionation of rare-earth elements by aqueous fuids upon slab dehydration. *Earth and Planetary Science Letters* 398, 101–112. https://doi.org/10.1016/j.epsl.2014.04.042

Uher P., Černý P., Chapman R., Határ J. & Miko O. 1998a: Evolution of Nb–Ta minerals in the Prašivá granitic pegmatites, Slovakia: I. Primary Fe, Ti-rich assemblage. *Canadian Mineralogist* 36, 525–534

Uher P., Černý P., Chapman R., Határ J. & Miko O. 1998b: Evolution of Nb–Ta minerals in the Prašivá granitic pegmatites, Slovakia: II. External hydrothermal Pb, Sb overprint. *Canadian Mineralogist* 36, 535–545.

Uher P., Broska I., Krzemińska E., Ondrejka M., Mikuš T. & Vaculovič T. 2019: Titanite composition and SHRIMP U–Pb dating as indicators of post-magmatic tectonothermal activity: Variscan I-type tonalites to granodiorites, the Western Carpathians. *Geologica Carpathica* 70, 449–470. https://doi.org/10.2478/geoca-2019-0026

van Lichtervelde M., Melcher F. & Wirth R. 2009: Magmatic vs. hydrothermal origins for zircon associated with tantalum mineralization in the Tanco pegmatite, Manitoba, Canada. *American Mineralogist* 94, 439–450. https://doi.org/10.2138/am.2009.2952

van Lichtervelde M., Goncalves P., Eglinger A., Colin A., Montel J.-M. & Dacheux N. 2021: Solubility of monazite–cheralite and xenotime in granitic melts, and experimental evidence of liquid–liquid immiscibility in concentrating REE. *Journal of Petrology* 62, egab020. https://doi.org/10.1093/petrology/egab020

Villaros A., Stevens G. & Buick I.S. 2009: Tracking S-type granite from source to emplacement: clues from garnet in the Cape Granite Suite. *Lithos* 112, 217–235. https://doi.org/10.1016/j.lithos.2009.02.011

Wang R.-C., Wang D.-Z., Zhao G.-T., Lu J.-J., Chen X.-M. & Xu S.-J. 2001: Accessory mineral record of magma-fluid interaction in the Laoshan I- and A-type granitic complex, Eastern China. *Physics and Chemistry of the Earth, Part A: Solid Earth and Geodesy* 26, 835–849. https://doi.org/10.1016/s1464-1895(01)00131-4

Wark D.A. & Miller C. 1993: Accessory mineral behavior during differentiation of a granite suite: monazite, xenotime, and zircon in the Sweetwater Wash pluton, southwastern California, U.S.A. *Chemical Geology* 110, 49–67. https://doi.org/10.1016/0009-2541(93)90247-G

Watson E.B. & Harrison T.M. 1984: Accessory minerals and the geochemical evolution of crustal magmatic systems: a summary and prospectus of experimental approaches. *Physics of the Earth and Planetary Interiors* 35, 19–30. https://doi.org/10.1016/0031-9201(84)90031-1

Williams-Jones A.E., Migdisiov A.A. & Samson I. 2012: Hydrothermal mobilisation of the rare earth elements – a tale of "ceria" and "yttria". *Elements* 8, 355–360. https://doi.org/10.2113/gselements.8.5.355

Electronic supplementary materials S1–S7 are available online:

http://geologicacarpathica.com/data/files/supplements/GC-74-5-Maraszewska_Suppl-S1.xlsx
http://geologicacarpathica.com/data/files/supplements/GC-74-5-Maraszewska_Suppl-S2.xlsx
http://geologicacarpathica.com/data/files/supplements/GC-74-5-Maraszewska_Suppl-S3.xlsx
http://geologicacarpathica.com/data/files/supplements/GC-74-5-Maraszewska_Suppl-S4.xlsx
http://geologicacarpathica.com/data/files/supplements/GC-74-5-Maraszewska_Suppl-S5.xlsx
http://geologicacarpathica.com/data/files/supplements/GC-74-5-Maraszewska_Suppl-S6.xlsx
http://geologicacarpathica.com/data/files/supplements/GC-74-5-Maraszewska_Suppl-S7.xlsx